# Comprehensive phylogenetic analysis of the ribonucleotide reductase family reveals an ancestral clade

Audrey A. Burnim<sup>1</sup>\*, Matthew A. Spence<sup>2</sup>\*, Da Xu<sup>1</sup>\*, Colin Jackson<sup>2,3,4†</sup>, and Nozomi Ando<sup>1†</sup>

<sup>1</sup>Department of Chemistry and Chemical Biology, Cornell University, Ithaca, NY 14850, USA. <sup>2</sup>Research School of Chemistry, Australian National University, Canberra, ACT, 2601, Australia. <sup>3</sup>Australian Research Council Centre of Excellence for Innovations in Peptide and Protein Science, Australian National University, Canberra, ACT 2601, Australia. <sup>4</sup>Australian Research Council Centre of Excellence in Synthetic Biology, Australian National University, Canberra, ACT 2601, Australia.

**Abstract.** Ribonucleotide reductases (RNRs) are used by all free-living organisms and many viruses to catalyze an essential step in the *de novo* biosynthesis of DNA precursors. RNRs are remarkably diverse by primary sequence and cofactor requirement, while sharing a conserved fold and radical-based mechanism for nucleotide reduction. Here, we structurally aligned the diverse RNR family by the conserved catalytic barrel to reconstruct the first large-scale phylogeny consisting of 6,779 sequences that unites all extant classes of the RNR family and performed evo-velocity analysis to independently validate our evolutionary model. With a robust phylogeny in-hand, we uncovered a novel, phylogenetically distinct clade that is placed as ancestral to the classes I and II RNRs, which we have termed clade Ø. We employed small-angle X-ray scattering (SAXS), cryogenic-electron microscopy (cryo-EM), and AlphaFold2 to investigate a member of this clade from *Synechococcus* phage S-CBP4 and report the most minimal RNR architecture to-date. Based on our analyses, we propose an evolutionary model of diversification in the RNR family and delineate how our phylogeny can be used as a roadmap for targeted future study.

<sup>\*</sup> These authors contributed equally to this work.

<sup>†</sup>Correspondence should be addressed to colin.jackson@anu.edu.au and nozomi.ando@cornell.edu.

#### Introduction

The wealth of genomic and metagenomic sequence data that has exploded in recent years provides a new opportunity to reexamine enzyme families using large-scale and robust bioinformatic analyses. A particularly important enzyme family that necessitates such analyses are the ribonucleotide reductases (RNRs). RNRs are used by all free-living organisms and many viruses for the conversion of ribonucleotides to 2'-deoxyribonucleotides in the *de novo* biosynthesis of DNA precursors (Torrents et al., 2002). RNRs are especially fascinating from an evolutionary perspective as they exhibit high diversity in primary sequence and cofactor requirement (Lundin et al., 2015), yet they share a common fold and radical-based catalytic mechanism for nucleotide reduction (Licht et al., 1996).

Based on current biochemical evidence, the full catalytic cycle is thought to involve three steps in all RNRs (**Figure 1** – figure supplement 1): cofactor-mediated generation of a thiyl radical at a conserved cysteine in the active site, nucleotide reduction, and re-reduction of the active site after turnover (Greene et al., 2020; Holmgren and Sengupta, 2010). Despite being a diverse enzyme family, the core structure of the catalytic subunit (known as  $\alpha$ ) is a conserved 10-stranded  $\alpha/\beta$  barrel with the thiyl radical on the so-called "finger loop" which connects the two halves of the barrel (Figure 1) (Uhlin and Eklund, 1996). RNRs have been biochemically classified into three major groups based on the cofactor used to generate the thiyl radical (**Figure 1** – figure supplement 1). Class I RNRs use a ferritin subunit ( $\beta$ ) to house a stable radical cofactor and are further subclassified by the metal content of the cofactor (Cotruvo and Stubbe, 2011; Ruskoski and Boal, 2021). For every turnover, the  $\alpha$  and  $\beta$  subunits must form a complex to engage in long-range radical transfer to the active site (Kang et al., 2020; Seyedsayamdost et al., 2007). In class II RNRs, the thiyl radical is generated by a 5'-deoxyadenosyl radical (5'-dAdo•) produced from an adenosylcobalamin (AdoCbl) cofactor bound within the active site, and thus these enzymes do not require additional subunits (Licht et al., 1996). In class III RNRs, the thiyl radical is generated by a glycyl radical on the C-terminal domain of the α subunit, which itself is generated by a separate activase enzyme that utilizes S-adenosylmethionine (AdoMet) bound to a [4Fe-4S] cluster for radical chemistry (Wei et al., 2014b). Once the thiyl radical is produced in the active site, nucleotide reduction proceeds via a conserved mechanism for all classes (Licht et al., 1996) (Figure 1 – figure supplement 1). In most RNRs, nucleotide reduction is coupled with the oxidation of a conserved pair of active-site cysteines (Figure 1 – figure supplement 1) (Booker et al., 1994; Mao et al., 1992; Wei et al., 2014a), which are ultimately reduced by a thioredoxin system to enable the next round of turnover, although some class III RNRs use formate to directly reduce the active site (Wei et al., 2014b).

Except for a subset of class II RNRs which are monomeric, all extant RNR α subunits are thought to dimerize at the αA and αB helices in their active forms. Class I and II RNRs dimerize in anti-parallel orientation at these helices, such that the dimer interface is capped on both ends with a functional insertion known as loop 1 (Figure 1B-C, dark green), which is the binding site for nucleotides that control the identity of the substrate in the active site (Larsson et al., 2004; Zimanyi et al., 2016). The binding of these so-called specificity-regulating effectors is coupled to substrate binding via another insertion known as loop 2 (Figure 1B-C, red) (Zimanyi et al., 2016). Class I and II RNRs also share another insertion, a long β-hairpin motif, between the αH helix and βH strand. Although less is known about the function of this insertion, it is thought to be important for binding the radical cofactor (the entire ferritin subunit in the case of class I RNRs and the AdoCbl cofactor in the case of class II RNRs) (Kang et al., 2020; Sintchak et al., 2002; Thomas et al., 2019). Class III RNRs, on the other hand, dimerize at the  $\alpha A$  and  $\alpha B$  helices such that they are oriented parallel to each other across the interface. This orientation is stabilized by a long helix in place of the loop 1 insertion (Logan et al., 1999) (Figure 1D, dark green). Additionally, the class III RNRs contain a glycyl radical domain with a zinc finger motif at the C-terminus. In contrast, the C-termini of class I and II RNRs that have been characterized are unstructured and contain cysteines to re-reduce the active-site cysteines via disulfide exchange (Booker et al., 1994; Mao et al., 1992; Thomas et al., 2019). Thus, overall, class I and II RNRs share more structural similarities with each other than they do with class III RNRs.

The ancestor of modern RNRs, and its subsequent evolution into the three known classes has long been of interest for its hypothesized importance in transitioning life from an RNA/protein world to a DNA world (Lundin et al., 2015, 2009; Poole et al., 2002; Reichard, 1993; Stubbe, 2000; Stubbe et al., 2001; Torrents, 2014; Torrents et al., 2002). Class I RNRs have been proposed to be the most recently evolved class as they require molecular oxygen, which became abundant as the Earth's atmosphere transitioned from anoxic to oxic. In contrast, class III RNRs have been proposed to have emerged before this transition as glycyl radicals and [4Fe-4S] clusters are both extremely oxygen-sensitive (Fontecave et al., 1989) and Fe-S chemistry is thought to have a prebiotic origin (Goldman and Kaçar, 2021). The AdoCbl chemistry used by class II RNRs, on the other hand, is neither oxygen-dependent nor especially oxygen sensitive. Based on the relative oxygen sensitivities and biosynthetic complexities of the different cofactors, class III RNRs have been proposed to be the most ancient of the RNR family (Reichard, 1997; Riera et al., 1997). However, whether class III predates class II has been debated when considering cofactor availability (Stubbe, 2000). Indeed, cobalamin, AdoMet, and Fe-S clusters have all been proposed to be part of the cofactor set used by the last universal common ancestor (LUCA) (Weiss et al., 2016). It has been proposed in an alternative model that dimeric class II and III RNRs evolved in parallel from a shared ancestor using class II-like chemistry and that class I RNRs then evolved from class II (Lundin et al., 2015). However, this model was derived from

a structure-based phylogenetic network (Bryant and Moulton, 2004), which estimates a phylogeny based on pairwise structural alignment scores rather than evolutionary modelling on protein sequences with well-established amino acid substitution models and statistical frameworks. Despite much effort to understand the diversity and evolution of RNRs, the reconstruction of a large-scale, unifying phylogenetic inference that includes all classes of RNRs has been hindered by the significant computational demand imposed by the high sequence diversity of the extant members of the family.

In this study, we used the conserved 10-stranded  $\alpha/\beta$  barrel to anchor highly diverged RNR sequences in a structure-based alignment and used maximum-likelihood inference to reconstruct the largest RNR phylogeny to-date, consisting of 6,779  $\alpha$  sequences, that unifies all classes. Our comprehensive phylogeny shows the parallel development of three major clades, corresponding to the three known classes, with a small, phylogenetically distinct clade, which we denote as class  $\varnothing$  (for convenience, pronounced "oh"), placed as an ancestral clade to the class I and II RNRs. Using small-angle X-ray scattering (SAXS), cryo-electron microscopy (cryo-EM) and AlphaFold2 (Jumper et al., 2021), we show that the class  $\varnothing$   $\alpha$  is the most minimal RNR structurally characterized thus far. These observations were corroborated by evo-velocity analysis, an alignment-independent method that employs protein language models to infer sequence fitness and evolutionary trajectories (Hie et al., 2022). Together, our analyses indicate that class III RNRs diverged early on and evolved independently of class I and II RNRs, which diverged from an ancestor shared with the minimal, class  $\varnothing$  RNRs. Our evolutionary model provides an explanation for the structural similarities of the class I and II RNRs and also supports the idea that adaptations to an oxygenated atmosphere appeared earlier than initially thought.

#### Results

# Phylogenetic reconstruction and evo-velocity analysis reveal the evolution of three RNR classes and a novel clade.

To study the molecular evolution of the RNR family, we performed comprehensive phylogenetic inference on the catalytic  $\alpha$  subunits (**Figure 2**). Unlike sequence analyses, such as sequence similarity network (SSN) analysis (Atkinson et al., 2009), which provide insight exclusively on the global similarities shared between extant sequences, phylogenetic inference delineates the evolutionary history of related sequences utilizing complex models of evolution that account for the rate of mutation of base pairs or amino acids. However, large-scale phylogenetic reconstruction on entire protein superfamilies is technically challenging and computationally demanding. Homology is often difficult to detect between extensively diverged proteins, complicating the generation of a robust sequence alignment, without which accurate topological reconstruction

and model parameterization cannot be achieved. To overcome these challenges, we adapted a recently developed workflow (Spence et al., 2021), which uses ensembles of hidden Markov models (HMMs) guided by structural information to build an accurate alignment of  $6,779 \,\alpha$  sequences that spans 5 PFAM families.

Phylogenetic reconstruction was performed by maximum-likelihood (ML) inference. Tree searches were performed with 10 replicates under the sequence evolution model LG+R10 (Kalyaanamoorthy et al., 2017; Le and Gascuel, 2008), which was selected by Akaike and Bayesian information criteria (Dridi and Hadzagic, 2019) on a representative subset of the full 6,779 RNR sequence dataset. To test the robustness of our phylogenetic hypotheses against model diversity, we inferred an additional 10 replicates of treesearch under an alternative general amino acid replacement matrix (WAG+R10) (Whelan and Goldman, 2001). Each of the 10 phylogenies inferred under LG+R10 failed rejection by the approximately unbiased (AU) test (Shimodaira, 2002) conducted to 10,000 replicates (lowest P-value = 0.283), including those whose branch supports failed to converge. All 20 inferences, irrespective of evolutionary model, converged on a similar phylogenetic topology. To further test the robustness of our results, we repeated our analyses at a redundancy threshold of 55% sequence identity, which yielded a topology with the same cladistic groupings as the full inference (Figure 2 – figure supplements 1 and 2), indicating that the likelihood surface of the evolutionary relationships of RNR α subunits has a well-defined global maximum that we had reached in our tree-searches. This was corroborated by high branch supports (ultrafast bootstrap approximation 2.0 and approximate likelihood ratio tests) for major bifurcations in each independent reconstruction, including deep nodes at the midpoint root of each tree (Figure 2B). The topology that is presented in Figure 2 had the highest branch supports at key nodes of interest in RNR evolution.

Consistent with our current understanding of RNR evolution, all reconstructed topologies that converged and failed rejection by the AU-test resolved the three biochemical classes of RNRs as monophyletic lineages (**Figure 2**, blue/yellow/red). Additionally, we find strong support for classes I and II diverging from a single common ancestor that shared an ancestor with the class III RNRs. We identified a novel clade of  $\alpha$  sequences that diverged from the last common ancestor (LCA) of classes I and II, which we denote as the class  $\emptyset$  clade (**Figure 2**, green). We note that there are two trees inferred from the LG+R10 dataset that do not resolve class  $\emptyset$  as a separate clade, where instead these sequences are a monophyletic clade diverging from class II sequences. Topology testing shows that although these trees are valid hypotheses, the  $\Delta$  log likelihood values indicate that they are the least likely trees of the 10 trees inferred under the LG+R10 model. Moreover, when we repeated phylogenetic reconstruction with a different sequence redundancy threshold, the topology with class  $\emptyset$  as an ancestral clade to classes I and II was reproduced independently (**Figure 2** – figure supplement 2). In the topology with the best statistical support, the branch that separates

the LCA of classes  $\emptyset$ , I, II from class III is the midpoint of the phylogeny. Rooting on this branch places class III as the most ancestral, followed by the emergence of the LCA of classes  $\emptyset$ , I, II and the subsequent divergence of classes I and II. Midpoint rooting is the best available method to understand the diversification of all RNRs in this instance, given that the tree unifies all classes of RNRs in the in-group and is well-balanced despite the diversity of sequences. The consistency in the location of the midpoint in the full-dataset phylogeny and the reduced redundancy phylogeny (**Figure 2** – figure supplements 1 and 2) further validates the choice to root on the midpoint.

As phylogenetic inference is susceptible to biases introduced by taxon sampling (Pollock et al., 2002), model parameterization and assumptions, sequence alignment (Simmons et al., 2011), and tree-search and because our choice to midpoint root the phylogeny assumes a constant evolutionary rate, we also used a recently described phylogeny-independent method known as evo-velocity analysis to test our phylogenetic hypotheses (Hie et al., 2022). Evo-velocity is a machine-learning analysis based on the principles of natural language processing (NLP) (Hie et al., 2022). NLP models such as ESM-1b, a >650,000,000 parameter NLP model trained on UniProt50 amino acid sequences (Rives et al., 2021), can embed query sequences in a high-dimensional space where likelihoods can be numerically computed as proxy fitness scores on a graph network. By assuming that the inherent directionality of the embedded sequence graph-network moves in the direction of evolution, as evolution compels proteins towards more fit (i.e., more probable in the NLP model) sequences, sequences with low learned probabilities can be interpreted as starting points in evolutionary trajectories. Evo-velocity thus bypasses many of the assumptions of phylogenetic inference as it is alignment independent, does not require model parameterization or tree-search, and has previously been used to validate conclusions based on superfamily-scale phylogenetic inference (Hie et al., 2022; Spence et al., 2021).

When projected onto a two-dimensional basis (see **Methods**), the ESM-1b embedded RNR graph network (**Figure 3**) shares many common topological features with the full family phylogeny (**Figure 2**). Class III RNRs (**Figure 3A**, red) belong to a diverged cluster of sequences that have evolved independently of class I and II sequences (**Figure 3A**, blue/yellow). Conversely, class I and II are joined over the same sequence space, indicating a common recent ancestor. The class Ø sequences occupy the interface between classes I and II (**Figure 3A**, green), consistent with their phylogenetic placement as ancestral to the class I/II lineage. Evo-velocity analysis also identified multiple roots in the RNR family (**Figure 3B**, dark purple). This is likely a consequence of sequences diverging over geological timescales and lacking intermediate phylogenetic information between major groups. The multiple roots belong to each of the major lineages, signifying independent evolution down distinct trajectories. However, pseudotime velocity, a proxy for phylogenetic

depth (Haghverdi et al., 2016), clearly captures the interface of class I and II sequences (including class  $\emptyset$ ) as the most ancestral within that lineage (**Figure 3C**). The congruence between phylogenetic and evovelocity analyses supports our hypotheses on the evolution of extant RNRs. The projection of class  $\emptyset$  sequences onto the ancestral interface of classes I and II additionally provides evidence that they indeed hold a pivotal position in RNR evolution.

# Class Ø RNRs are predominantly found in marine bacteria and cyanophages

The class  $\emptyset$  clade consists of RNRs from both bacteria and phages, many of which are phototrophs. Nearly half of the sequences in the clade were obtained from cyanophages (**Figure 4A**, bolded species) or uncultured phages, while the remainder were obtained from marine bacteria, including those collected in the *Tara* Oceans Expedition (Tully et al., 2018). Performing a BLAST search of photosynthetic genes, such as *psbA* and *psbD*, against the genomes (of which many are incomplete) of the 35 bacteria and phages listed in the clade yielded 11 hits (**Figure 4A**, species in green).

The classification of the cyanophage sequences observed in this clade (Figure 4A, bolded species) has been previously debated (Harrison et al., 2019). These RNRs from cyanosipho- and cyanopodoviruses were initially annotated as class II, based on studies of the *Prochlorococcus* phage P-SSP7 genome, which contains two consecutive genes that were proposed to represent a split RNR with homology to class II RNRs (Dwivedi et al., 2013; Lindell et al., 2005; Sullivan et al., 2005). More recently, it was discovered that these two genes encode for an RNR a subunit and a small ferritin-like protein and were thus reannotated as class I (Harrison et al., 2019). However, in the phylogenetic analysis reported in this previous study, the cyanophage a sequences fell in either the class I or class II clades depending on the stringency for homology used for grouping the sequences. This result contrasts with our work, where the class Ø clade is phylogenetically distinct from the other major clades (Figure 2). Additionally, we find that all completely sequenced operons with a class Ø RNR a gene (24/35 in Figure 4A) contain a small ferritin-like gene (annotated with InterPro family number for the ferritin-like superfamily IPR009078) immediately downstream (Figure 4 – figure supplement 1), and thus, we find that this feature is not exclusive to cyanophages. Interestingly, an all-vs-all pBLAST search of every class Ø sequence against all class I sequences in our phylogeny detects poor homology (E-value > 0.05) (Figure 4B, blue), while querying class Ø RNRs against class II returns hundreds of significant hits (E-value < 10E-10) (Figure 4B, yellow). Thus, by sequence homology, class Ø RNRs appear to be more class-II like despite being associated with a ferritin-like gene that is reminiscent of class I RNRs, which supports the phylogenetic results indicting they are a distinct class.

### Class Ø RNRs are minimal and share features of class I and II enzymes.

The class  $\varnothing$  lineage consists of  $\alpha$  sequences with an average length of 412 amino acids, which are significantly shorter than those of the class Id catalytic subunit that were previously described as having a minimal architecture with a median length of 565 amino acids (Rose et al., 2019). Like the class Id  $\alpha$  sequences, the class  $\varnothing$  sequences all lack a ~100-residue ATP-cone motif at the N-terminus, which is used for allosteric regulation of overall activity in many other RNRs (Meisburger et al., 2017). Additionally, the class  $\varnothing$  C-terminus contains a double cysteine motif, which is likely used for reducing a pair of active-site cysteines that are oxidized following every turnover. Of the 24 class  $\varnothing$  sequences that are complete at the C-terminus, 10 contain a CXXC motif and 14 contain a CXC motif (where aspartic acid is the most common middle amino acid). The sequences that appear to be incomplete at the C-terminus largely belong to uncultured phages. The C-terminal CXXC motif is a common feature of class I RNRs (found in 1737 of 2022 class I sequences in our dataset), but the CXC motif is rare among both class I and II RNRs. Only seven class I sequences and one class II sequence in our dataset appear to have a CXC motif. The prevalence of this motif makes the class  $\varnothing$  RNRs unlike class I or II RNRs. Interestingly, the CXXC-containing sequences are most ancestral within the class  $\varnothing$  clade, while the more recently evolved sequences have the CXC motif.

To examine the structural features of the class Ø RNR, we used a combination of AlphaFold2, SAXS, and cryo-EM to characterize the *Synechococcus* phage S-CBP4 α subunit. Importantly, this α sequence is highly representative of the clade, scoring an E-value of 1.2E-228 on an HMM sequence profile of each class Ø sequence. In the absence of nucleotides, our SAXS profiles are consistent with a monomer-dimer equilibrium (**Figure 4** – figure supplement 2) where the S-CBP4  $\alpha$  subunit is predominantly monomeric at low protein concentrations (≤4 µM). Addition of substrate (guanosine diphosphate, GDP) does not shift this equilibrium, but the presence of the corresponding specificity effector (thymidine triphosphate, TTP), strongly favors dimerization (Figure 4 – figure supplement 2A-B). This result is consistent with TTP binding the specificity site to stabilize the same dimeric form adopted by class I and II  $\alpha$  subunits. Using solution conditions that saturate nucleotide binding (200 µM TTP, 200 µM GDP), we obtained a cryo-EM map of the S-CBP4  $\alpha_2$  dimer to 3.46-Å resolution (Fourier shell correlation, FSC = 0.143) (**Figure 4C**, **Figure 4** – figure supplement 3). An atomic model (residues 22-426 out of 470) was refined against the cryo-EM map using an AlphaFold2 prediction as the starting model (Table 1). The final refined model was highly similar to the starting model with a root mean square deviation (all-atom RMSD) of 1.44 Å. The elongated shape of the S-CBP4  $\alpha_2$  dimer observed by cryo-EM (**Figure 4D**, red dashed curve) explains the distinct flattened region in our experimental SAXS profile between  $q \sim 0.05$  - 0.15 Å<sup>-1</sup> (**Figure 4D**, blue curve), and excellent model-data agreement is observed over the full q-range when the disordered N- and C-termini are included in the model (**Figure 4D**, black dashed curve and blue curve).

Overall, the S-CBP4 \alpha subunit displays the most minimal RNR architecture discovered to-date with few insertions about the catalytic barrel (Figure 4 – figure supplement 4). The minimal set of insertions includes traits shared by class I and II RNRs, such as loop 1, where we find cryo-EM density for bound TTP (Figure **4E**). Additionally, the S-CBP4  $\alpha$  subunit contains a long  $\beta$ -hairpin following the  $\beta$ H strand of the catalytic barrel that in class II RNRs is thought to be important for cofactor binding (Sintchak et al., 2002) and in class I RNRs is thought to be important for interactions with the β subunit (Kang et al., 2020). Although we do not observe density for the C-terminus past the βJ strand of the catalytic barrel, two consecutive tyrosine residues (Y420 and Y421) on βJ are well-resolved and stacked adjacent to the catalytic cysteine (C185) at the tip of finger loop (Figure 4F). In class I RNRs, this stacked arrangement of the tyrosine dyad is required for long-range proton-coupled electron transfer (PCET) between the  $\beta$  subunit and the catalytic cysteine (Greene et al., 2017) (Figure 4 – figure supplement 5A). By comparison, inspection of existing structures (Larsson et al., 2010; Sintchak et al., 2002) suggests that in class II RNRs, the space between the βJ strand and the finger-loop cysteine forms a pocket to accommodate the adenosyl group of the cobalamin cofactor (Figure 4 – figure supplement 5B). We note that the appearance of the double tyrosine motif does not necessarily indicate that an RNR a sequence belongs to class I. In fact, there are class II sequences with this motif, but structure prediction of these sequences indicate that the double tyrosine motif is placed outside of the binding pocket for adenosyl group, rather than filling this space (Figure 4 – figure supplement 5C). Finally, we observe a disulfide between active-site cysteines (C30 and C196) that in class I and II RNRs serve as reducing equivalents during nucleotide reduction (Figure 4G). Consistent with an oxidized active site, cryo-EM density for the substrate is not observed. This in turn explains why residues 13-20 are disordered in our cryo-EM model, as it is predicted to form a helix involved in substrate binding (Figure 1A, gray helix adjacent to left star).

Although the class  $\emptyset$  a subunit contains a tyrosine dyad poised for PCET like class I a subunits, the class  $\emptyset$  ferritin-like sequences are significantly shorter (average length of 240 amino acids) than those of *bona fide* class I  $\beta$  subunits (average length of 346 amino acids). Querying each complete class  $\emptyset$  ferritin-like sequence returns only a single homologous sequence over the whole length of the alignment (all hits E-value > 1E-4, excluding one) when searched against PFAM families PF00210 (ferritin-like proteins, 17,981 entries) and PF00268 (class I RNR  $\beta$  subunit, 9,898 entries). However, based on AlphaFold2, which detects more than sequence homology, class  $\emptyset$  ferritin-like proteins resemble class I  $\beta$  subunits with shorter insertions and termini (**Figure 4** – figure supplement 6A-D). As in class I  $\beta$  subunits, the class  $\emptyset$  proteins are predicted to contain a core ferritin fold consisting of two helix-turn-helices (**Figure 4** – figure supplement 6A and 6C, red/pink and yellow/green), each contributing an E/D + EXXH metal-binding motif (Ruskoski

and Boal, 2021). Additionally, while most class I  $\beta$  sequences have a tyrosine serving as the site of the radical downstream of the first metal-binding motif (**Figure 1** – figure supplement 1), class Ø ferritin-like proteins contain a redox-inert residue (Phe or Leu) at this site, much like class Ic RNRs (Bollinger et al., 2008; Cotruvo and Stubbe, 2011) (**Figure 4** – figure supplement 6E). Class Ø ferritin-like sequences also contain a C-terminal tyrosine (Y239 in **Figure 4** – figure supplement 6A), which in class I RNRs is involved in inter-subunit radical transfer (Y356 in **Figure 4** – figure supplement 6C). However, the C-termini of the class Ø ferritin-like proteins are unusually short, terminating at the residue downstream from this tyrosine, and lack the ~10-residue extension that class I  $\beta$  subunits use for binding to the  $\alpha$  subunit. Thus, although the class Ø ferritin-like proteins are likely to use a similar radical-generating mechanism as class I  $\beta$  subunits, they may interact with the  $\alpha$  subunit different manner to enable PCET. However, ongoing biochemical work to confirm this has thus far been nontrivial as the class Ø ferritin-like proteins can be unstable in the absence of metals, most likely because of their small size. This makes characterization of metal dependence more challenging as it means that the metal composition cannot be easily varied. Further investigation will be the focus of future work. Regardless, the class Ø  $\alpha$  structure illustrates how the class I and II RNRs may have inherited shared traits from a common ancestor.

#### **Discussion**

As RNR sequences have been diverging for billions of years, pair-wise sequence identity is frequently low (<15%), and sequence homology is often undetectable between distant members of the enzyme family. It is therefore challenging to produce an accurate sequence alignment of all RNR classes, without which a phylogenetic inference cannot be performed. Thus, although various models for RNR evolution have been proposed by biochemical reasoning (e.g., based on the availabilities and oxygen sensitivities of the cofactors), prior to our work, phylogenetic inference had only been performed on a very small scale. Early studies included an inference of 8 class II sequences (Jordan et al., 1997) performed with Clustal W (Thompson et al., 1994) and an inference with a dataset of 96 class I, II, and III sequences (Torrents et al., 2002). In the latter study, Torrents and co-workers used a neighbor-joining (NJ) algorithm to build a tree using a Poisson model, which assumes that all amino acids have equal probability of change (Torrents et al., 2002). The NJ approach can be understood as a way to build a tree by creating nodes between pairs of sequences that are considered close by a certain metric for distance, which in this case is determined by the Poisson sequence evolution model. This approach differs significantly from modern methods of tree inference in which the tree topology is determined by the sequence evolution model itself (Minh et al., 2020) often in replicate. Furthermore, the sequence availability at the time was too sparse to capture the true diversity of the RNR family, and the dataset lacked class Ø sequences, monomeric class II sequences, as well as many subclasses of the class I sequences.

Since then, small-scale inferences have been performed on subsets of the RNR family on either the  $\alpha$  or  $\beta$  subunit with datasets ranging between 10s to 100s of sequences in size (Dwivedi et al., 2013; Lundin et al., 2010; Martínez-Carranza et al., 2020; Rose et al., 2019; Rozman Grinberg et al., 2018; Sakowski et al., 2014). Among these, the work of Lundin and co-workers has been the most comprehensive with respect to consideration of the different RNR classes (Lundin et al., 2010). The growth of sequence information, however, also meant that greater diversity had to be accounted for by phylogenetic methods, and therefore, phylogenetic inference had not been performed on all RNR classes simultaneously since the seminal work of Torrents, et al. In its place, a structure-based phylogenetic network was constructed via an NJ algorithm, where the distance between two sequences was estimated by pairwise structural alignment scores (Lundin et al., 2015). Under the assumption that this network estimates a phylogenetic tree, different possible roots were considered, and although none led to monophyly of the RNR classes, it was proposed that the class I RNRs emerged from the dimeric class II RNRs.

In this study, we succeeded in performing a large-scale phylogenetic reconstruction of the entire, highly diverse RNR family for the first time by using structural information to aid the sequence alignment procedure. To test for alternative hypotheses, we performed maximum-likelihood inference using two different amino acid replacement matrices in replicate (10 trees for each model) and repeated the inference with a different sequence redundancy threshold to test for the effect of taxon sampling on tree topology and evolutionary conclusions. Key bifurcations featured high branch supports and reproducibility in replicate tree inferences, allowing us to make robust interpretations, which were further supported by evo-velocity analysis, a recently introduced method that is independent of multiple sequence alignments (Hie et al., 2022). In contrast to previously proposed models (Lundin et al., 2015), our unified RNR phylogeny supports the evolution of three major, monophyletic clades corresponding to the three biochemically known classes as well as a new phylogenetic clade, which we denoted as class Ø. Together, our bioinformatic analyses support an evolutionary trajectory in which the O<sub>2</sub>-sensitive class III RNRs are the earliest to diverge, and the class Ø clade shares an ancestor with the LCA of the O<sub>2</sub>-dependent class I and O<sub>2</sub>-tolerant class II RNRs. It is important to note that all evolutionary models, including ours, are hypotheses, and it is impossible to know the true historical trajectory of mutations. Nonetheless, we can say that the evolutionary conclusions we present in this work were derived from the most advanced approach that is currently possible, and with the strongest statistical support and congruence across multiple independent methods. This work highlights the advances we have seen in bioinformatic methods while also providing a roadmap for the many important questions that remain.

Most notably, our phylogeny revealed the novel class Ø clade, which is exclusively (among characterized organisms) associated with marine microbes, such as cyanophages and photosynthetic bacteria. Bioinformatically, we showed that the class Ø a subunit shares significant sequence homology with class II sequences, while also containing in its gene neighborhood a gene for a ferritin-like protein that resembles the class I  $\beta$  subunit. Structurally, we further showed that the class  $\emptyset$  a subunit defines the minimum set of features shared by class I and II RNRs, including the orientation of the two monomers in the dimer, specificity site at loop 1, and the β-hairpin. It was previously hypothesized that the LCA of RNRs may have possessed class II-like biochemistry based on the Precambrian bioavailabilities of iron and cobalt and the abiotic synthesis of porphyrin rings (Lundin et al., 2015). An alternative hypothesis is supported by our phylogeny, which places the class I mechanism as ancestral to, or having diverged in parallel with, that of class II. Although we cannot classify the mechanism of radical generation in the class Ø RNRs in the absence of biochemical data, our phylogeny suggests that a class II-like enzyme resembling the extant class Ø sequences recruited a ferritin-like protein into the catalytic machinery, before diverging into class I RNRs (which retained a ferritin subunit for catalysis) and class II RNRs (which specialized in cobalamin usage). The usage of a ferritin-like protein in class Ø RNRs is supported by the observation of a stacked YY dyad in the active site of our cryo-EM structure, which suggests that long-range radical transfer is an important component of catalysis in these enzymes. However, the short C-terminus of the class Ø ferritins and the prevalence of the CXC motif in the a C-terminus suggest that there are key differences with the class I and II RNRs. Future biochemical characterization will require identification of the correct metallocofactors for activity and possible reducing partners.

Based on our results, we present the following model for the evolution of the RNR family. The LCA of the RNR catalytic subunit likely shared the most biochemical resemblance to extant class III RNRs. Increasing oxygen availability selected for the divergence of the RNR family into the anaerobic LCA of class III and the oxygen-tolerant LCA of classes Ø – II, from which the minimal class Ø RNRs diverged. Class I and II RNRs sharing an ancestor would suggest that multiple strategies to adapt to the presence of oxygen evolved in parallel, rather than sequentially. Interestingly, we find sequences from the earliest diverging cyanobacterium, *Gloeobacter*, near the root of the class II clade in our phylogeny. *Gloeobacter* are notable for lacking thylakoid membranes and have been called "the missing link" between anoxic photosynthesis, which involves Fe-S chemistry, and oxygenic photosynthesis (Nakamura et al., 2003; Saw et al., 2013). Thus, along with the emergence of cyanobacteria (Schirrmeister et al., 2013), it is possible that class II RNRs evolved well before the Great Oxygenation Event (GOE). If so, this would imply that class I RNRs also emerged before the Earth's atmosphere became permanently oxidizing. In fact, recent work suggests that oxygen availability was sufficient for the birth of O<sub>2</sub>-producing and O<sub>2</sub>-utilizing enzymes to occur well before the

geochemically defined GOE (Jabłońska and Tawfik, 2021). Such an evolutionary model could explain how O<sub>2</sub>-dependent class I RNRs can share an ancestor with class II RNRs. In this respect, it is especially intriguing that class Ø RNRs are associated with cyanophages and photosynthetic bacteria.

### Outlook

With a unifying RNR phylogeny, we propose an evolutionary model with implications for the early emergence of molecular adaptations to oxygen. Our phylogeny also directs new avenues of study. We expect biochemical studies of the class Ø clade to provide insight into how an ancestral radical-generating mechanism may have diverged into class I and II mechanisms. We also anticipate that by analyzing the extensions and insertions about the catalytic barrel, we will gain a greater understanding of how allosteric and catalytic mechanisms evolved within the RNR family. Finally, with a phylogenetic inference, it is conceivable that we will be able to reconstruct ancestral sequences and gain detailed insight into evolutionary trajectories. In all, our unifying RNR phylogeny will guide future studies to fill important gaps in our everevolving understanding of this family of complex enzymes.

#### Methods

#### Sequence collection and SSN analysis

A dataset of 105,904 sequences belonging to families PF02867, PF08343, PF13597, PF00317, PF17975, and PF08471 was downloaded from the PFAM server (El-Gebali et al., 2019). The computational complexity of phylogenetic reconstruction increases exponentially with the number of taxa sampled in the inference. A sequence redundancy threshold of 85% was imposed on the dataset, and redundant sequences were clustered and represented as a single sequence in CD-HIT (Fu et al., 2012) to both balance taxon sampling across divergent lineages and reduce the computational complexity of the inference. Because the PFAM database typically features many sequences that are truncated, incomplete or are part of larger multidomain proteins, we removed all sequences that were smaller or larger than 400 or 1100 residues (the expected upper and lower bounds for RNR sequences based on prior data and characterized proteins), respectively. An all-vs-all pBLAST search was performed for each sequence in the dataset using default search parameters and an E-value threshold of 10E<sup>-240</sup>. The search result was visualized as a force-directed graph network in Cytoscape (Hie et al., 2021; Shannon et al., 2003). The final non-redundant dataset consisted of 12,968 sequences.

# Sequence alignment

As RNR sequences have been diverging for billions of years, pair-wise sequence identity is frequently low (<15%), and homology is often undetectable between distant members of the superfamily. Conventional

alignment algorithms failed to align these large and diverse datasets, which were evaluated against structural alignments of phylogenetically diverse RNRs. Instead, we employed our recently reported workflow (Spence et al., 2021) that uses ensembles of HMMs that are iteratively trained on increasingly diverse sequences until the full diversity of the dataset is captured. The initial HMM in this workflow captures residues that are tolerated at each site of the consensus RNR fold. This HMM was built from a non-redundant structural alignment of 9 diverse RNR crystal structures (1h78, 4coj, 3o0m, 6cgm, 1pem, 5im3, 3hne, 3s87, and 2x0x) that had been aligned in MUSTANG (Konagurthu et al., 2010) HMMs were built using the HMMBuild application of the HMMer suite (Finn et al., 2011). Sequences from each SSN cluster were scored against a cluster-specific HMM, which was generated in HMMer from all sequences within that cluster. The E-value that a sequence scores against the HMM of the cluster that it belongs to therefore serves as a metric for how representative that sequence is to the overall cluster. The most representative sequence from each sequence cluster in the SSN was aligned to the initial structural HMM (755 sequences).

This "representative" alignment, and a corresponding maximum-likelihood (ML) phylogenetic tree that was reconstructed in IQ-TREE (Minh et al., 2020) was used as a seed alignment and guide tree, respectively, for the full alignment of all non-redundant RNR sequences. The final sequence alignment was performed in UPP from the SEPP alignment package (Nguyen et al., 2015). As this alignment workflow exploits structural information, residues that are not crystallographically resolved or residues that do not align, such as non-conserved insertions and N-/C- terminal extensions (including the ATP cone), are not included in the alignment. The full alignment was manually refined by removing non-conserved insertions (typically single residue insertions conserved in fewer than 1% of sequences) and poorly aligned sequences that are unlikely to be functional RNRs. The final alignment features 6,779 RNR sequences.

### Phylogenetic reconstruction

The RNR superfamily phylogeny was reconstructed by ML from the full RNR alignment. Phylogenetic inference was performed using IQ-TREE2.0 (Minh et al., 2020) on the Australian National Computing Infrastructure (NCI) GADI supercomputer and BioHPC servers at the Cornell Institute of Biotechnology. Stochastic tree-search was conducted with a stochastic perturbation strength of 0.2 to a maximum of 2000 iterations. Convergence was defined as 200 iterations of tree-search that failed to improve the current best tree. Branch supports were measured by ultrafast bootstrap approximation 2.0 (Hoang et al., 2018) and the approximate likelihood ratio test, each conducted to 10,000 replicates. The sequence evolution model, LG replacement matrix (Le and Gascuel, 2008) with a 10 category free-rate rate heterogeneity model (Kalyaanamoorthy et al., 2017), was determined by ML using ModelFinder (Kalyaanamoorthy et al., 2017) as implemented in IQ-TREE2.0 on the representative sequence alignment. To test the robustness of our

hypotheses against model uncertainty, we performed an additional 10 replicates of ML tree-search using an alternate general amino-acid replacement matrix (WAG+R10) (Whelan and Goldman, 2001). The AU-test conducted to 10,000 replicates was used to compare all tree topologies (Shimodaira, 2002). To further test the robustness of our hypotheses against taxon sampling, we performed an additional and independent phylogenetic reconstruction on a sequence dataset with redundancy removed to 55% sequence identity. As with the full inference, the 55% redundancy phylogeny was inferred in IQ-TREE 2.0 under LG+R10.

#### ESM-1b evo-velocity modeling

Protein natural language processing (NLP) models can provide valuable and phylogeny-independent evolutionary insight (Alley et al., 2019; Hie et al., 2021; Rives et al., 2021). The 6,779 sequences in our dataset were embedded as high-dimensional vectors in the ESM-1b protein language model (Rives et al., 2021) and projected onto a two-dimensional directed network graph with uniform manifold approximation and projection (UMAP) (McInnes, L., Healy, J., Saul, N., & Großberger, L., 2018). Likelihoods along each edge in the network graph were computed and visualized as a vector field. Under the assumption that likelihoods inferred from the NLP model are correlated with evolutionary fitness, the vector field "flows" in the direction of evolution, and pseudotime velocity is correlated with phylogenetic depth (Hie et al., 2021).

### Expression and purification of Synechococcus phage S-CBP4 a subunit

The gene for the  $\alpha$  subunit of *Synechococcus* phage S-CBP4 RNR was synthesized by Genscript with a His<sub>6</sub>-SUMO (smt3) tag at the N-terminus and cloned into a pET-28c+ vector in between the *NcoI* and *XhoI* cloning sites. His<sub>6</sub>-smt3-tagged- $\alpha$  was grown overnight at 37 °C with 200 rpm shaking in 100 mL of LB medium supplemented with 50 µg/mL kanamycin. Large-scale growth was initiated by adding 10 mL of saturated starter culture to six 1 L volumes of kanamycin-supplemented LB medium incubating at 37 °C with 200 rpm shaking. At an OD<sub>600</sub> of 0.4, IPTG was added to a final concentration of 0.4 mM, and cultures were shaken at 37 °C 200 rpm for 6 hours. Cells were harvested by centrifugation at 4 °C (15 min at 3,500 x g), frozen in liquid nitrogen, and stored at -80 °C.

All steps of purification were completed at 4 °C. The cell pellet was placed on ice and thawed for 30 min prior to resuspension in Buffer A: 50 mM sodium phosphate, pH 7.6, 300 mM NaCl, 2 mM imidazole, 5% (v/v) glycerol and 1 mM tris(2-carboxyethyl)phosphine (TCEP). For lysis, Buffer A was supplemented with 5 U mL<sup>-1</sup> DNase, 5 U mL<sup>-1</sup> RNase A and 0.2 mg mL<sup>-1</sup> lysozyme (hen egg white, Sigma), 1.5 mM MgCl<sub>2</sub>, and EDTA-free protease inhibitor tablet (Roche), 250 μM phenylmethylsulfonyl fluoride (PMSF). Cells were homogenized with a French Press at 14,000 psi for 10 minutes inside a cold room operating at 4 °C. Cell debris was separated by centrifugation at 4 °C (25,000 x g, 30 min), and the supernatant was loaded

onto a Talon cobalt affinity column (5 mL bed volume) equilibrated in Buffer A. The column was washed with the equilibration buffer for 10 column volumes, and protein was eluted with Buffer A with 500 mM imidazole. Protein-containing fractions were pooled and buffer exchanged into Buffer A via a centrifugal concentrator (30 kDa Amicon). Smt3-protease was added of a 350:1 mole ratio of tagged protein:Smt3 protease. Detagged protein was collected via the flowthrough of a second cobalt affinity column equilibrated with Buffer A. Further purification was performed with size exclusion chromatography on a HiLoad Superdex 200 pg preparative 16/600 column in Buffer A. All protein concentrations are given as monomer concentrations. All biophysical studies were performed in the following assay buffer except where noted in the cryo-EM sample preparation: 50 mM HEPES pH 7.6, 150 mM NaCl, 15 mM MgCl<sub>2</sub>, 1 mM TCEP and 5% (v/v) glycerol.

# Small-angle X-ray scattering

X-ray scattering experiments were performed at the Cornell High Energy Synchrotron Source (CHESS) ID7A1 station. Data were collected using a 250  $\mu$ m x 200  $\mu$ m X-ray beam with an energy of 9.9 keV and a flux of ~10<sup>12</sup> photons s<sup>-1</sup> mm<sup>-1</sup> at the sample position. Small-angle X-ray scattering (SAXS) images were collected on an Eiger 4M detector covering a range of q = 0.009–0.55 Å<sup>-1</sup>. Here, the momentum transfer variable is defined as q=4 $\pi$ / $\lambda$  sin $\theta$ , where  $\lambda$  is the X-ray wavelength and 2 $\theta$  is the scattering angle. Data processing at the beamline was performed in BioXTAS RAW (Hopkins et al., 2017). Briefly, scattering images were integrated about the beam center and normalized by transmitted intensities measured on a photodiode beamstop. The integrated protein scattering profile, I(q), was produced by subtraction of background buffer scattering from the protein solution scattering. Radii of gyration ( $R_g$ ) were estimated with Guinier analysis, and pair distance distribution analysis was performed with Bayesian indirect Fourier transformation (BIFT) (Hansen, 2000). Error bars associated with  $R_g$  values are curve-fitting uncertainties from Guinier analysis. Subsequent analysis was performed in MATLAB and utilized REGALS and other established protocols (Meisburger et al., 2021, 2016; Skou et al., 2014)

The scattering of *Synechococcus* phage S-CBP4  $\alpha$  subunit was first measured over the concentration range of 4 – 40  $\mu$ M. 8  $\mu$ M was chosen for subsequent titration of nucleotides to maintain near physiological concentration (Ando et al., 2011; Parker, 2017). For all titration experiments, background subtraction was performed with carefully matched buffer solutions containing identical concentrations of nucleotides following established protocols (Skou et al., 2014). For each measurement, 40  $\mu$ L of sample were prepared fresh and centrifuged at 14,000×g at 4 °C for 10 min immediately before loading into an in-vacuum flow cell kept at 4 °C. For each protein and buffer solution, 20 × 2 s exposures were taken with sample oscillation to limit radiation damage then averaged together to improve signal. SVD was performed in MATLAB.

Size-exclusion chromatography-coupled SAXS (SEC–SAXS) experiments were performed using a Superdex 200 Increase 10/300 GL (24 mL) column operated by a GE Akta Purifier at 4 °C with the elution flowing directly into an in-vacuum X-ray sample cell. To account for a ~10-fold dilution of the sample during elution, 40  $\mu$ L sample was prepared at 80  $\mu$ M protein in assay buffer with 200  $\mu$ M TTP and 200  $\mu$ M GDP for substrate. Sample was then centrifuged at 14,000×g for 10 min at 4 °C before loading onto a column pre-equilibrated in a matched buffer containing 200  $\mu$ M TTP, 200  $\mu$ M GDP. Samples were eluted at flow rates of 0.05 mL min<sup>-1</sup> and 2-s exposures were collected throughout elution until the elution profile had returned to buffer baseline. Normalized, integrated scattering profiles were binned 6-fold in frame number and 4-fold in q, and scattering profiles of the elution buffer were averaged to produce a background-subtracted SEC–SAXS dataset. Singular value decomposition (SVD) was performed to determine the number of significant components, and the SEC-SAXS dataset was decomposed in the MATLAB implementation of REGALS (Meisburger et al., 2021).

Structural modeling was performed using the ATSAS package (Manalastas-Cantos et al., 2021) and Allos-ModFoXS (Schneidman-Duhovny et al., 2010; Weinkam et al., 2012) following previously established protocols (Ando et al., 2011, 2016; Meisburger et al., 2016; Thomas et al., 2019). Theoretical scattering curves of the cryo-EM model (Methods described below, PDB: 7urg) were calculated in CRYSOL (Svergun et al., 1995) with 50 spherical harmonics, 256 points between 0 and 0.5 Å–1, and the default electron density of water. The overall scale factor and solvation parameters were determined by fitting to the protein scattering curve extracted by REGALS. Disordered and missing residues were modeled in AllosModFoXS (Konarev et al., 2003; Manalastas-Cantos et al., 2021) with sampling of static structures consistent with the starting model.

# Cryo-EM grid preparation and data acquisition

QuantiFoil holey carbon R 1.2/1.3 300-mesh grids were glow discharged on a PELCO easiGlow system for 45 s with 15 mA current. Grid freezing was then performed on a FEI Vitrobot Mark IV with the chamber humidity set to 100% and the temperature set to 4 °C. 3  $\mu$ L of sample (4  $\mu$ M *Synechococcus* phage S-CBP4  $\alpha$  subunit in 50 mM HEPES pH 7.6, 150 mM NaCl, 7.55 mM MgCl<sub>2</sub>, 200  $\mu$ M TTP, 200  $\mu$ M GDP, 1 mM TCEP, 1% v/v glycerol) was applied onto the grid. The sample was blotted for 4 s and then immediately plunged into liquid ethane cooled by liquid nitrogen.

Data collection was performed at the Cornell Center for Materials Research (CCMR) on a Talos Arctica (Thermo Fisher Scientific) operating at 200 keV with a Gatan K3 direct electron detector and BioQuantum

energy filter at a nominal magnification of 79,000 x (1.07 Å/pixel). A total of 856 movies was collected with a nominal defocus range from -0.6  $\mu$ m to -2.0  $\mu$ m and a total dose of 50 e<sup>-</sup>/Å<sup>2</sup> over 50 frames (2.164 s total exposure time, 0.0435 s frame time, 26.96 e<sup>-</sup>/Å<sup>2</sup>/s dose rate).

### Cryo-EM data processing

Initial processing was performed in cryoSPARC v3.3.1 (Punjani et al., 2017). Patch motion correction and patch CTF estimation were performed on 856 movies. The resulting micrographs were manually curated based on statistics and visual inspection, and 432 micrographs were retained. 46 high quality micrographs were then selected, from which the blob picker routine was used to pick particles. The resulting 99k particles were extracted and subjected to 2D classification, and the top four unique 2D classes were selected and used as templates for template picking on the entire dataset. Due to the large variance in ice conditions in many of our micrographs, masks were manually defined for every micrograph, and particle picks outside the ideal ice region were excluded. The resulting 582k particles were extracted with a box size of 256 pixels binned to 128 pixels. Two rounds of 2D classification were performed, and only particles corresponding to the top 2D classes with secondary structure features were kept. The 203k remaining particles were re-extracted with 256-pixel box size and subjected to ab initio reconstruction and heterogeneous refinement into two classes. The top class containing 117k particles was then subjected to homogeneous refinement with C2 symmetry, which yielded a 4.04 Å map. Duplicate particles were removed using a minimum separation distance of 80 Å, and the remaining particles (108k) were subjected to a non-uniform refinement (Punjani et al., 2020) with C2 symmetry imposed and per-particle defocus and CTF parameter optimization enabled, which yielded a 3.57 Å map.

To employ Bayesian polishing in RELION-3 (Zivanov et al., 2018), the same 432 micrographs were motion-corrected in RELION 3.1 using its own implementation of MotionCorr2 (Zheng et al., 2017) with 5 by 5 patches. The particle .cs file from the cryoSPARC non-uniform refinement job was converted to star format using pyem (Asarnow, D., Palovcak, E., & Cheng, Y., 2019) with the micrograph path modified to that of the RELION motion-corrected micrographs. Particles were then re-extracted from RELION motion-corrected micrographs with a box size of 256 pixels. Due to the failure of RELION 3D auto-refine to converge on a reasonable structure from these particles, particles were imported back into cryoSPARC and subjected to homogeneous refinement. The particle .cs file from this refinement job was again converted to a star file using pyem. Relion\_reconstruct was employed to reconstruct two half maps using the offset and angle information refined in cryoSPARC with the same half data split, and post-processing was performed on the resulting half maps using the refinement mask from cryoSPARC. Bayesian polishing (Zivanov et al., 2019) training and polishing jobs were then performed with this post-processing job as input. The

resulting shiny particles were successfully refined to a 3.85 Å map with 3D auto-refine in RELION. After one round of CTF refinement (Zivanov et al., 2020) the particles were subjected to another round of Bayesian polishing, and the resulting shiny particles were imported back into cryoSPARC. Non-uniform refinement on shiny particles with C2 symmetry imposed and per-particle defocus and CTF parameter optimization enabled yielded the final 3.46-Å resolution map used for model building and analysis.

# AlphaFold prediction and atomic model building

The sequence for the *Synechococcus* phage S-CBP4  $\alpha$  subunit was retrieved from UniProt (Bateman et al., 2021) with accession number M1PRZ0. The sequence was used as input for AlphaFold2 prediction (Jumper et al., 2021) with the five default model parameters and a template date cutoff of 2020-05-14. As the five models were largely identical in the core region and differing only in the location of the C-terminal tail, the structure predicted with the first model parameter was used in the subsequent process.

The predicted structure of the *Synechococcus* phage S-CBP4 α subunit was first processed and docked into the unsharpened cryo-EM map in phenix. The 25 N-terminal residues and 45 C-terminal residues were then manually removed due to lack of cryo-EM density, and residues 26-426 were retained in the model. We observed unmodeled density at the specificity site, and based on solution composition, we modeled a TTP molecule. A structure of TTP coordinating a magnesium ion was extracted from the crystal structure of *Bacillus subtilis* RNR (pdb: 6mt9) (Thomas et al., 2019) and rigid body fit into the unmodeled density in Coot (Emsley and Cowtan, 2004). The combined model was refined with unsharpened and sharpened maps using phenix.real\_space\_refine (Afonine et al., 2018; Liebschner et al., 2021), with a constraint applied on the magnesium ion coordinated by the triphosphate in TTP according to the original configuration. Residue and loop conformations in the resulting structure were manually adjusted in Coot to maximize fit to map and input for an additional round of real-space refinement in phenix with an additional restraint for the disulfide bond between C30 and C196. The atomic coordinates and maps have been deposited to the Protein Data Bank and EM Data Bank under accession codes 7urg and EMD-26712. Due to the weak density for the magnesium ion, it was removed from the atomic coordinates when deposited into PDB.

#### EM Data collection, processing, and refinement

Data collection and processing	
Microscope	Talos Arctica
Camera	K3

Magnification	79,000
Voltage (keV)	200
Electron exposure (e <sup>-</sup> /Å <sup>2</sup> )	50
Defocus range (μm)	-0.6 to -2.0
Pixel size (Å)	1.07
Micrographs used (no.)	432
Initial particles (no.)	581,884
Final particles (no.)	107,885
Symmetry imposed	C2
Map resolution (Å) FSC threshold	3.46 (0.143)
Map resolution range (Å)	3.0 – 7.0 (75%)
Refinement	
Initial model used	AlphaFold2 prediction for UniProt entry M1PRZ0
Model resolution (Å) FSC threshold	3.6 (0.5)
Map sharpening B factor (Å <sup>2</sup> )	-171
Model composition Non-hydrogen atoms Protein residues Ligands	6260 802 TTP
B factors (Ų)  Protein  Ligand	74.37 67.23
R.m.s. deviations  Bond lengths (Å)  Bond angles (°)	0.004 0.937
Validation  MolProbity score Clashscore Poor rotamers (%)	1.47 4.69 0.00
Ramachandran plot Favored (%) Allowed (%) Disallowed (%)	96.49 3.51 0.00

# Data Availability

The cryo-EM map has been deposited in the Electron Microscopy Data Bank under accession code EMD-26712, and the model has been deposited in the Protein Data Bank under accession code 7urg. The phylogeny shown in Figure 2 is available at (<a href="https://itol.embl.de/shared/yFvz6aVgum9z">https://itol.embl.de/shared/yFvz6aVgum9z</a>). The structure-guided sequence alignment and all twenty inferred phylogenies are available for download as supplementary materials.

#### **Author Contributions**

NA and CJ conceived of the project, designed and supervised research, and analyzed data. AAB performed bioinformatic analyses, purified and expression protein, performed SAXS analysis, and analyzed and curated all project results. MS devised bioinformatic workflow, performed computational experiments, and assisted in data analysis and manuscript preparation. DX performed AlphaFold predictions and cryo-EM data acquisition and analysis. AAB, DX, and NA wrote the paper with contributions from MS and CJ. All authors edited the manuscript.

# Acknowledgments

The authors are grateful to Drs. Will Thomas and Steve Meisburger for helpful discussions and Drs. Richard Gillilan and Qingqiu Huang for assistance at the 1D7A beamline at CHESS. SAXS was conducted at the Center for High Energy X-ray Sciences (CHEXS), which is supported by the National Science Foundation (NSF) under award DMR-1829070, and the Macromolecular Diffraction at CHESS (MacCHESS) facility, which is supported by award 1-P30-GM124166-01A1 from the National Institute of General Medical Sciences (NIGMS), National Institutes of Health (NIH), and by New York State's Empire State Development Corporation (NYSTAR). Cryo-EM work was done using the Cornell Center for Materials Research (CCMR) Shared Facilities, which are supported through the NSF MRSEC program (DMR-1719875). This project was undertaken with the assistance of resources and services from the National Computational Infrastructure (NCI), which is supported by the Australian Government, as well as with the BioHPC resource at the Cornell Institute of Biotechnology. We acknowledge the ARC Centre of Excellence for Innovations in Peptide and Protein Science (CE200100012), the ARC Centre of Excellence in Synthetic Biology (CE200100029). This work was supported by NSF grant MCB-1942668 (to N.A.) and startup funds from Cornell University (to N.A.).

#### References

Afonine PV, Poon BK, Read RJ, Sobolev OV, Terwilliger TC, Urzhumtsev A, Adams PD. 2018. Real-space refinement in PHENIX for cryo-EM and crystallography. *Acta Crystallogr D Struct Biol* **74**:531–544.

- Alley EC, Khimulya G, Biswas S, AlQuraishi M, Church GM. 2019. Unified rational protein engineering with sequence-based deep representation learning. *Nat Methods* **16**:1315–1322.
- Ando N, Brignole EJ, Zimanyi CM, Funk MA, Yokoyama K, Asturias FJ, Stubbe J, Drennan CL. 2011. Structural interconversions modulate activity of Escherichia coli ribonucleotide reductase. *Proc Natl Acad Sci U S A* **108**:21046–21051.
- Ando N, Li H, Brignole EJ, Thompson S, McLaughlin MI, Page JE, Asturias FJ, Stubbe J, Drennan CL. 2016. Allosteric Inhibition of Human Ribonucleotide Reductase by dATP Entails the Stabilization of a Hexamer. *Biochemistry* **55**:373–381.
- Asarnow, D., Palovcak, E., & Cheng, Y. 2019. asarnow/pyem: UCSF pyem v0.5. doi:10.5281/zenodo.3576630
- Atkinson HJ, Morris JH, Ferrin TE, Babbitt PC. 2009. Using sequence similarity networks for visualization of relationships across diverse protein superfamilies. *PLoS One* **4**:e4345.
- Bateman A, Martin MJ, Orchard S, Magrane M, Agivetova R, Ahmad S, Alpi E, Bowler-Barnett EH, Britto R, Bursteinas B, Bye-A-Jee H, Coetzee R, Cukura A, Silva AD, Denny P, Dogan T, Ebenezer TG, Fan J, Castro LG, Garmiri P, Georghiou G, Gonzales L, Hatton-Ellis E, Hussein A, Ignatchenko A, Insana G, Ishtiaq R, Jokinen P, Joshi V, Jyothi D, Lock A, Lopez R, Luciani A, Luo J, Lussi Y, MacDougall A, Madeira F, Mahmoudy M, Menchi M, Mishra A, Moulang K, Nightingale A, Oliveira CS, Pundir S, Qi G, Raj S, Rice D, Lopez MR, Saidi R, Sampson J, Sawford T, Speretta E, Turner E, Tyagi N, Vasudev P, Volynkin V, Warner K, Watkins X, Zaru R, Zellner H, Bridge A, Poux S, Redaschi N, Aimo L, Argoud-Puy G, Auchincloss A, Axelsen K, Bansal P, Baratin D, Blatter MC, Bolleman J, Boutet E, Breuza L, Casals-Casas C, de Castro E, Echioukh KC, Coudert E, Cuche B, Doche M, Dornevil D, Estreicher A, Famiglietti ML, Feuermann M, Gasteiger E, Gehant S, Gerritsen V, Gos A, Gruaz-Gumowski N, Hinz U, Hulo C, Hyka-Nouspikel N, Jungo F, Keller G, Kerhornou A, Lara V, Le Mercier P, Lieberherr D, Lombardot T, Martin X, Masson P, Morgat A, Neto TB, Paesano S, Pedruzzi I, Pilbout S, Pourcel L, Pozzato M, Pruess M, Rivoire C, Sigrist C, Sonesson K, Stutz A, Sundaram S, Tognolli M, Verbregue L, Wu CH, Arighi CN, Arminski L, Chen C, Chen Y, Garavelli JS, Huang H, Laiho K, McGarvey P, Natale DA, Ross K, Vinayaka CR, Wang Q, Wang Y, Yeh LS, Zhang J. 2021. UniProt: The universal protein knowledgebase in 2021. Nucleic Acids Res 49:D480–D489.
- Blaesi EJ, Palowitch GM, Hu K, Kim AJ, Rose HR, Alapati R, Lougee MG, Kim HJ, Taguchi AT, Tan KO, Laremore TN, Griffin RG, Krebs C, Matthews ML, Silakov A, Bollinger JM, Allen BD, Boal AK. 2018. Metal-free class Ie ribonucleotide reductase from pathogens initiates catalysis with a tyrosine-derived dihydroxyphenylalanine radical. *Proc Natl Acad Sci U S A* 115:10022–10027.
- Bollinger JM Jr, Jiang W, Green MT, Krebs C. 2008. The manganese(IV)/iron(III) cofactor of Chlamydia trachomatis ribonucleotide reductase: structure, assembly, radical initiation, and evolution. *Curr Opin Struct Biol* **18**:650–657.
- Booker S, Licht S, Broderick J, Stubbe JA. 1994. Participation of Five Cysteine Residues in Ribonucleotide Reductiont. *Biochemistry* **33**:12676–12685.
- Bryant D, Moulton V. 2004. Neighbor-net: an agglomerative method for the construction of phylogenetic networks. *Mol Biol Evol* **21**:255–265.
- Cotruvo JA, Stubbe J. 2011. Class I ribonucleotide reductases: metallocofactor assembly and repair in vitro and in vivo. *Annu Rev Biochem* **80**:733–767.
- Dridi N, Hadzagic M. 2019. Akaike and Bayesian Information Criteria for Hidden Markov Models. *IEEE Signal Process Lett* **26**:302–306.
- Dwivedi B, Xue B, Lundin D, Edwards RA, Breitbart M. 2013. A bioinformatic analysis of ribonucleotide reductase genes in phage genomes and metagenomes.
- El-Gebali S, Mistry J, Bateman A, Eddy SR, Luciani A, Potter SC, Qureshi M, Richardson LJ, Salazar GA, Smart A, Sonnhammer ELL, Hirsh L, Paladin L, Piovesan D, Tosatto SCE, Finn RD. 2019. The Pfam protein families database in 2019. *Nucleic Acids Res* **47**:D427–D432.
- Emsley P, Cowtan K. 2004. Coot: model-building tools for molecular graphics. *Acta Crystallogr D Biol Crystallogr* **60**:2126–2132.

- Finn RD, Clements J, Eddy SR. 2011. HMMER web server: interactive sequence similarity searching. *Nucleic Acids Res* **39**:W29-37.
- Fontecave M, Eliasson R, Reichard P. 1989. Oxygen-sensitive ribonucleoside triphosphate reductase is present in anaerobic Escherichia coli. *Proc Natl Acad Sci U S A* **86**:2147–2151.
- Fu L, Niu B, Zhu Z, Wu S, Li W. 2012. CD-HIT: accelerated for clustering the next-generation sequencing data. *Bioinformatics* **28**:3150–3152.
- Goldman AD, Kaçar B. 2021. Cofactors are Remnants of Life's Origin and Early Evolution. *J Mol Evol* **89**:127–133.
- Greene BL, Kang G, Cui C, Bennati M, Nocera DG, Drennan CL, Stubbe J. 2020. Ribonucleotide Reductases: Structure, Chemistry, and Metabolism Suggest New Therapeutic Targets. *Annu Rev Biochem* **89**:45–75.
- Greene BL, Taguchi AT, Stubbe J, Nocera DG. 2017. Conformationally dynamic radical transfer within ribonucleotide reductase. *J Am Chem Soc* **139**:16657–16665.
- Haghverdi L, Büttner M, Wolf FA, Buettner F, Theis FJ. 2016. Diffusion pseudotime robustly reconstructs lineage branching. *Nat Methods* **13**:845–848.
- Hansen S. 2000. Bayesian estimation of hyperparameters for indirect Fourier transformation in small-angle scattering. *J Appl Crystallogr* **33**:1415–1421.
- Harrison AO, Moore RM, Polson SW, Wommack KE. 2019. Reannotation of the ribonucleotide reductase in a cyanophage reveals life history strategies within the virioplankton. *Front Microbiol* **10**. doi:10.3389/fmicb.2019.00134
- Hie B, Zhong ED, Berger B, Bryson B. 2021. Learning the language of viral evolution and escape. *Science* **371**:284–288.
- Hie BL, Yang KK, Kim PS. 2022. Evolutionary velocity with protein language models predicts evolutionary dynamics of diverse proteins. *Cell Syst.* doi:10.1016/j.cels.2022.01.003
- Hoang DT, Chernomor O, von Haeseler A, Minh BQ, Vinh LS. 2018. UFBoot2: Improving the Ultrafast Bootstrap Approximation. *Mol Biol Evol* **35**:518–522.
- Holmgren A, Sengupta R. 2010. The use of thiols by ribonucleotide reductase. *Free Radic Biol Med* **49**:1617–1628.
- Hopkins JB, Gillilan RE, Skou S. 2017. BioXTAS RAW: improvements to a free open-source program for small-angle X-ray scattering data reduction and analysis. *J Appl Crystallogr* **50**:1545–1553.
- Jabłońska J, Tawfik DS. 2021. The evolution of oxygen-utilizing enzymes suggests early biosphere oxygenation. *Nat Ecol Evol* **5**:442–448.
- Jordan A, Torrents E, Jeanthon C, Eliasson R, Hellman U, Wernstedt C, Barbé J, Gibert I, Reichard P. 1997. B12-dependent ribonucleotide reductases from deeply rooted eubacteria are structurally related to the aerobic enzyme from Escherichia coli. *Proc Natl Acad Sci U S A* **94**:13487–13492.
- Jumper J, Evans R, Pritzel A, Green T, Figurnov M, Ronneberger O, Tunyasuvunakool K, Bates R, Žídek A, Potapenko A, Bridgland A, Meyer C, Kohl SAA, Ballard AJ, Cowie A, Romera-Paredes B, Nikolov S, Jain R, Adler J, Back T, Petersen S, Reiman D, Clancy E, Zielinski M, Steinegger M, Pacholska M, Berghammer T, Bodenstein S, Silver D, Vinyals O, Senior AW, Kavukcuoglu K, Kohli P, Hassabis D. 2021. Highly accurate protein structure prediction with AlphaFold. *Nature* **596**:583–589.
- Kalyaanamoorthy S, Minh BQ, Wong TKF, von Haeseler A, Jermiin LS. 2017. ModelFinder: fast model selection for accurate phylogenetic estimates. *Nat Methods* **14**:587–589.
- Kang G, Taguchi AT, Stubbe J, Drennan CL. 2020. Structure of a trapped radical transfer pathway within a ribonucleotide reductase holocomplex. *Science* **368**:424–427.
- Konagurthu AS, Reboul CF, Schmidberger JW, Irving JA, Lesk AM, Stuckey PJ, Whisstock JC, Buckle AM. 2010. MUSTANG-MR structural sieving server: applications in protein structural analysis and crystallography. *PLoS One* **5**:e10048.
- Konarev PV, Volkov VV, Sokolova AV, Koch MHJ, Svergun DI. 2003. PRIMUS: a Windows PC-based system for small-angle scattering data analysis. *J Appl Crystallogr* **36**:1277–1282.

- Larsson K-M, Jordan A, Eliasson R, Reichard P, Logan DT, Nordlund P. 2004. Structural mechanism of allosteric substrate specificity regulation in a ribonucleotide reductase. *Nat Struct Mol Biol* 11:1142–1149.
- Larsson K-M, Logan DT, Nordlund P. 2010. Structural basis for adenosylcobalamin activation in AdoCbldependent ribonucleotide reductases. *ACS Chem Biol* **5**:933–942.
- Le SQ, Gascuel O. 2008. An improved general amino acid replacement matrix. *Mol Biol Evol* **25**:1307–1320.
- Licht S, Gerfen GJ, Stubbe J. 1996. Thiyl radicals in ribonucleotide reductases. Science 271:477–481.
- Liebschner D, Afonine PV, Moriarty NW, Poon BK, Chen VB, Adams PD. 2021. CERES: a cryo-EM rerefinement system for continuous improvement of deposited models. *Acta Crystallogr D Struct Biol* 77:48–61.
- Lindell D, Jaffe JD, Johnson ZI, Church GM, Chisholm SW. 2005. Photosynthesis genes in marine viruses yield proteins during host infection. *Nature* **438**:86–89.
- Logan DT, Andersson J, Sjöberg BM, Nordlund P. 1999. A glycyl radical site in the crystal structure of a class III ribonucleotide reductase. *Science* **283**:1499–1504.
- Lundin D, Berggren G, Logan D, Sjöberg B-M. 2015. The Origin and Evolution of Ribonucleotide Reduction. *Life* **5**:604–636.
- Lundin D, Gribaldo S, Torrents E, Sjöberg B-M, Poole AM. 2010. Ribonucleotide reduction horizontal transfer of a required function spans all three domains. *BMC Evol Biol* **10**:383.
- Lundin D, Torrents E, Poole AM, Sjöberg B-M. 2009. RNRdb, a curated database of the universal enzyme family ribonucleotide reductase, reveals a high level of misannotation in sequences deposited to Genbank. *BMC Genomics* **10**:589.
- Manalastas-Cantos K, Konarev PV, Hajizadeh NR, Kikhney AG, Petoukhov MV, Molodenskiy DS, Panjkovich A, Mertens HDT, Gruzinov A, Borges C, Jeffries CM, Svergun DI, Franke D. 2021. ATSAS 3.0: expanded functionality and new tools for small-angle scattering data analysis. *J Appl Crystallogr* **54**:343–355.
- Mao SS, Holler TP, Yu GX, Bollinger JM, Booker S, Johnston MI, Stubbe J. 1992. A model for the role of multiple cysteine residues involved in ribonucleotide reduction: Amazing and still confusing. *Biochemistry* **31**:9733–9743.
- Martínez-Carranza M, Jonna VR, Lundin D, Sahlin M, Carlson LA, Jemal N, Högbom M, Sjöberg BM, Stenmark P, Hofer A. 2020. A ribonucleotide reductase from clostridium botulinum reveals distinct evolutionary pathways to regulation via the overall activity site. *J Biol Chem* **295**:15576–15587.
- McInnes, L., Healy, J., Saul, N., & Großberger, L. 2018. UMAP: Uniform Manifold Approximation and Projection. *Journal of Open Source Software* **3**:861.
- Meisburger SP, Taylor AB, Khan CA, Zhang S, Fitzpatrick PF, Ando N. 2016. Domain Movements upon Activation of Phenylalanine Hydroxylase Characterized by Crystallography and Chromatography-Coupled Small-Angle X-ray Scattering. *J Am Chem Soc* **138**:6506–6516.
- Meisburger SP, Thomas WC, Watkins MB, Ando N. 2017. X-ray Scattering Studies of Protein Structural Dynamics. *Chemical Reviews*. doi:10.1021/acs.chemrev.6b00790
- Meisburger SP, Xu D, Ando N. 2021. REGALS: a general method to deconvolve X-ray scattering data from evolving mixtures. *IUCrJ* 8:225–237.
- Minh BQ, Schmidt HA, Chernomor O, Schrempf D, Woodhams MD, von Haeseler A, Lanfear R. 2020. IQ-TREE 2: New Models and Efficient Methods for Phylogenetic Inference in the Genomic Era. *Mol Biol Evol* **37**:1530–1534.
- Nakamura Y, Kaneko T, Sato S, Mimuro M, Miyashita H, Tsuchiya T, Sasamoto S, Watanabe A, Kawashima K, Kishida Y, Kiyokawa C, Kohara M, Matsumoto M, Matsuno A, Nakazaki N, Shimpo S, Takeuchi C, Yamada M, Tabata S. 2003. Complete genome structure of Gloeobacter violaceus PCC 7421, a cyanobacterium that lacks thylakoids. *DNA Res* **10**:137–145.
- Nguyen N-PD, Mirarab S, Kumar K, Warnow T. 2015. Ultra-large alignments using phylogeny-aware profiles. *Genome Biol* **16**:124.

- Parker MJ. 2017. Discovery and Investigation of the Novel Overall Activity Allosteric Regulation of the Bacillus subtilis Class Ib Ribonucleotide Reductase (Doctor of Philosophy in Biological Chemistry). Massachusetts Institute of Technology.
- Pollock DD, Zwickl DJ, McGuire JA, Hillis DM. 2002. Increased taxon sampling is advantageous for phylogenetic inference. *Syst Biol* **51**:664–671.
- Poole AM, Logan DT, Sjöberg BM. 2002. The evolution of the ribonucleotide reductases: Much ado about oxygen. *J Mol Evol* **55**:180–196.
- Punjani A, Rubinstein JL, Fleet DJ, Brubaker MA. 2017. cryoSPARC: algorithms for rapid unsupervised cryo-EM structure determination. *Nat Methods* **14**:290–296.
- Punjani A, Zhang H, Fleet DJ. 2020. Non-uniform refinement: adaptive regularization improves single-particle cryo-EM reconstruction. *Nat Methods* **17**:1214–1221.
- Reichard P. 1997. The evolution of ribonucleotide reduction. Trends Biochem Sci 22:81-85.
- Reichard P. 1993. The anaerobic ribonucleotide reductase from Escherichia coli. *J Biol Chem* **268**:8383–8386
- Riera J, Robb FT, Weiss R, Fontecave M. 1997. Ribonucleotide reductase in the archaeon Pyrococcus furiosus: A critical enzyme in the evolution of DNA genomes? *Proc Natl Acad Sci U S A* **94**:475–478.
- Rives A, Meier J, Sercu T, Goyal S, Lin Z, Liu J, Guo D, Ott M, Zitnick CL, Ma J, Fergus R. 2021. Biological structure and function emerge from scaling unsupervised learning to 250 million protein sequences. *Proc Natl Acad Sci U S A* **118**:e2016239118.
- Rose HR, Maggiolo AO, McBride MJ, Palowitch GM, Pandelia M-E, Davis KM, Yennawar NH, Boal AK. 2019. Structures of Class Id Ribonucleotide Reductase Catalytic Subunits Reveal a Minimal Architecture for Deoxynucleotide Biosynthesis **58**:49.
- Rozman Grinberg I, Lundin D, Hasan M, Crona M, Jonna VR, Loderer C, Sahlin M, Markova N, Borovok I, Berggren G, Hofer A, Logan DT, Sjöberg BM. 2018. Novel ATP-cone-driven allosteric regulation of ribonucleotide reductase via the radical-generating subunit. *Elife* 7. doi:10.7554/eLife.31529
- Ruskoski TB, Boal AK. 2021. The periodic table of ribonucleotide reductases. J Biol Chem 297:101137.
- Sakowski EG, Munsell EV, Hyatt M, Kress W, Williamson SJ, Nasko DJ, Polson SW, Wommack KE. 2014. Ribonucleotide reductases reveal novel viral diversity and predict biological and ecological features of unknown marine viruses. *Proc Natl Acad Sci U S A* 111:15786–15791.
- Saw JHW, Schatz M, Brown MV, Kunkel DD, Foster JS, Shick H, Christensen S, Hou S, Wan X, Donachie SP. 2013. Cultivation and complete genome sequencing of Gloeobacter kilaueensis sp. nov., from a lava cave in Kīlauea Caldera, Hawai'i. *PLoS One* **8**:e76376.
- Schirrmeister BE, de Vos JM, Antonelli A, Bagheri HC. 2013. Evolution of multicellularity coincided with increased diversification of cyanobacteria and the Great Oxidation Event. *Proc Natl Acad Sci U S A* **110**:1791–1796.
- Schneidman-Duhovny D, Hammel M, Sali A. 2010. FoXS: a web server for rapid computation and fitting of SAXS profiles. *Nucleic Acids Res* **38**:W540-4.
- Seyedsayamdost MR, Chan CTY, Mugnaini V, Stubbe J, Bennati M. 2007. PELDOR spectroscopy with DOPA-beta2 and NH2Y-alpha2s: distance measurements between residues involved in the radical propagation pathway of E. coli ribonucleotide reductase. *J Am Chem Soc* **129**:15748–15749.
- Shannon P, Markiel A, Ozier O, Baliga NS, Wang JT, Ramage D, Amin N, Schwikowski B, Ideker T. 2003. Cytoscape: A Software Environment for Integrated Models. *Genome Res* **13**:2498–2504.
- Shimodaira H. 2002. An approximately unbiased test of phylogenetic tree selection. *Syst Biol* **51**:492–508. Simmons MP, Müller KF, Webb CT. 2011. The deterministic effects of alignment bias in phylogenetic inference. *Cladistics* **27**:402–416.
- Sintchak MD, Arjara G, Kellogg BA, Stubbe JA, Drennan CL. 2002. The crystal structure of class II ribonucleotide reductase reveals how an allosterically regulated monomer mimics a dimer. *Nat Struct Biol* **9**:293–300.

- Skou S, Gillilan RE, Ando N. 2014. Synchrotron-based small-angle X-ray scattering of proteins in solution. *Nat Protoc* **9**:1727–1739.
- Spence MA, Mortimer MD, Buckle AM, Minh BQ, Jackson CJ. 2021. A comprehensive phylogenetic analysis of the serpin superfamily. *Mol Biol Evol*. doi:10.1093/molbev/msab081
- Srinivas V, Lebrette H, Lundin D, Kutin Y, Sahlin M, Lerche M, Eirich J, Branca RMM, Cox N, Sjöberg B-M, Högbom M. 2018. Metal-free ribonucleotide reduction powered by a DOPA radical in Mycoplasma pathogens. *Nature* **563**:416–420.
- Stubbe J. 2000. Ribonucleotide reductases: the link between an RNA and a DNA world? *Curr Opin Struct Biol* **10**:731–736.
- Stubbe J, Ge J, Yee CS. 2001. The evolution of ribonucleotide reduction revisited. *Trends Biochem Sci* **26**:93–99.
- Sullivan MB, Coleman ML, Weigele P, Rohwer F, Chisholm SW. 2005. Three Prochlorococcus cyanophage genomes: signature features and ecological interpretations. *PLoS Biol* **3**:e144.
- Svergun D, Barberato C, Koch MHJ. 1995. CRYSOL a Program to Evaluate X-ray Solution Scattering of Biological Macromolecules from Atomic Coordinates. *J Appl Crystallogr* **28**:768–773.
- Thomas WC, Brooks FP, Burnim AA, Bacik JP, Stubbe JA, Kaelber JT, Chen JZ, Ando N. 2019. Convergent allostery in ribonucleotide reductase. *Nat Commun* **10**:2653.
- Thompson JD, Higgins DG, Gibson TJ. 1994. CLUSTAL W: improving the sensitivity of progressive multiple sequence alignment through sequence weighting, position-specific gap penalties and weight matrix choice. *Nucleic Acids Res* 22:4673–4680.
- Torrents E. 2014. Ribonucleotide reductases: essential enzymes for bacterial life. *Front Cell Infect Microbiol* **4**:52.
- Torrents E, Aloy P, Gibert I, Rodríguez-Trelles F. 2002. Ribonucleotide reductases: divergent evolution of an ancient enzyme. *J Mol Evol* **55**:138–152.
- Tully BJ, Graham ED, Heidelberg JF. 2018. The reconstruction of 2,631 draft metagenome-assembled genomes from the global oceans. *Sci Data* **5**:170203.
- Uhlin U, Eklund H. 1996. The ten-stranded beta/alpha barrel in ribonucleotide reductase protein R1. *J Mol Biol* **262**:358–369.
- Wei Y, Funk MA, Rosado LA, Baek J, Drennan CL, Stubbe J. 2014a. The class III ribonucleotide reductase from Neisseria bacilliformis can utilize thioredoxin as a reductant. *Proc Natl Acad Sci U S A* **111**:E3756-65.
- Wei Y, Mathies G, Yokoyama K, Chen J, Griffin RG, Stubbe J. 2014b. A chemically competent thiosulfuranyl radical on the Escherichia coli class III ribonucleotide reductase. *J Am Chem Soc* **136**:9001–9013.
- Weinkam P, Pons J, Sali A. 2012. Structure-based model of allostery predicts coupling between distant sites. *Proc Natl Acad Sci U S A* **109**:4875–4880.
- Weiss MC, Sousa FL, Mrnjavac N, Neukirchen S, Roettger M, Nelson-Sathi S, Martin WF. 2016. The physiology and habitat of the last universal common ancestor. *Nat Microbiol* 1:16116.
- Whelan S, Goldman N. 2001. A general empirical model of protein evolution derived from multiple protein families using a maximum-likelihood approach. *Mol Biol Evol* **18**:691–699.
- Zheng SQ, Palovcak E, Armache J-P, Verba KA, Cheng Y, Agard DA. 2017. MotionCor2: anisotropic correction of beam-induced motion for improved cryo-electron microscopy. *Nat Methods* **14**:331–332.
- Zimanyi CM, Chen PYT, Kang G, Funk MA, Drennan CL. 2016. Molecular basis for allosteric specificity regulation in class ia ribonucleotide reductase from Escherichia coli. *Elife* 5:e07141.
- Zivanov J, Nakane T, Forsberg BO, Kimanius D, Hagen WJ, Lindahl E, Scheres SH. 2018. New tools for automated high-resolution cryo-EM structure determination in RELION-3. *Elife* 7. doi:10.7554/eLife.42166
- Zivanov J, Nakane T, Scheres SHW. 2020. Estimation of high-order aberrations and anisotropic magnification from cryo-EM data sets in RELION-3.1. *IUCrJ* 7:253–267.

Zivanov J, Nakane T, Scheres SHW. 2019. A Bayesian approach to beam-induced motion correction in cryo-EM single-particle analysis. *IUCrJ* **6**:5–17.

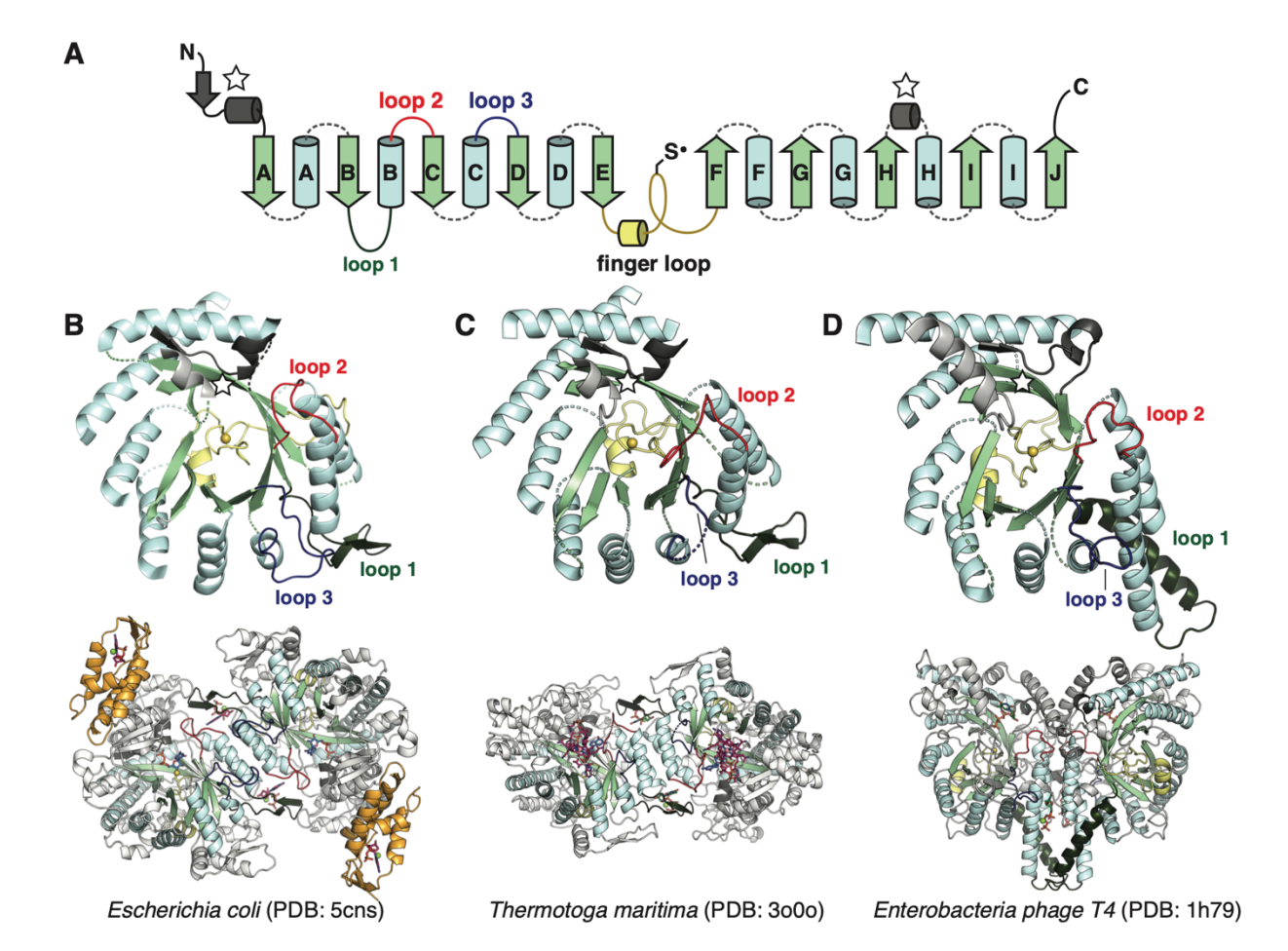


**Figure 1.** The catalytic fold of the ribonucleotide reductase (RNR) family is a unique 10-stranded  $\alpha/\beta$  barrel, consisting of ten β-strands (light green) and eight α-helices (light blue). (**A**) Each half of the barrel contains a 5-stranded parallel β-sheet (βA-βE and βF-βJ) that is arranged in anti-parallel orientation with respect to each other. The two halves are connected by the so-called "finger loop" (yellow) which typically begins with a short α-helix and contains a conserved cysteine that has been shown to be the site of the catalytically essential thiyl radical in all biochemically characterized RNRs. Diversity among the RNRs is generated by N- and C-terminal extensions as well as the insertions (dashed curves) between the secondary structure elements in the  $\alpha/\beta$  barrel. Loops 1-3 (dark green, red, blue) have special names in the RNR literature for their involvement in specificity regulation. The gray secondary structure elements (starred) are partially integrated in the  $\alpha/\beta$  barrel and are involved in substrate binding. (**B**) The barrel portion (top) of the *E. coli* class Ia catalytic subunit (bottom dimer). The ATP-cone domain is colored in orange. (**C**) The barrel portion

(top) of the *T. maritima* class II catalytic subunit (bottom dimer). (**D**) The barrel portion (top) of the T4 phage class III catalytic subunit (bottom dimer). In class III RNRs, the loop 1 region (dark green) is a long helix that is involved in dimerization.

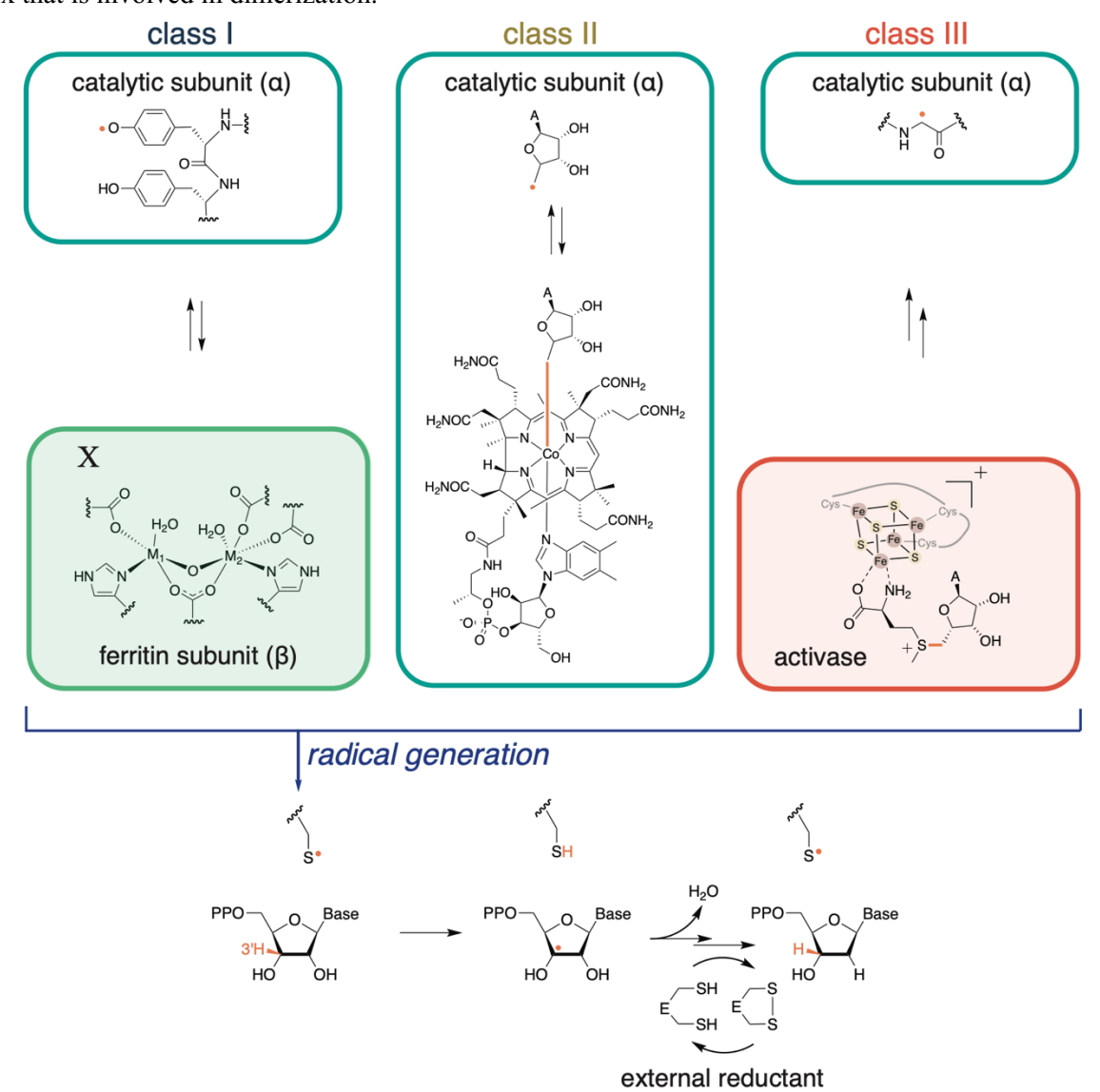


**Figure 1 – figure supplement 1.** RNRs catalyze the reduction of ribonucleoside di- or tri-phosphates (NDPs or NTPs) to their respective deoxynucleotide forms (dNDPs or dNTPs). The full catalytic cycle involves three steps: (1) cofactor-mediated generation of a thiyl radical, (2) nucleotide reduction, and (3) active-site reduction. In the first step, class I RNRs utilize a ferritin subunit, which has a characteristic metal-binding E/D + EXXH motif and a nearby residue, X. The residue X and the metal center together constitute the radical cofactor in class I RNRs. In most subclasses, X is a tyrosine, but it can also be a redoxinert residue like phenylalanine (e.g., as in class Ic RNRs) or a tyrosine post-translationally modified to dihydroxyphenylalaninine (DOPA) in class Ie RNRs. The metal ions (M1, M2) are typically Fe and/or Mn, although in class Ie RNRs, the metal-binding motif is not conserved and therefore unable to coordinate metals (Blaesi et al., 2018; Srinivas et al., 2018). Once the thiyl radical is generated, nucleotide reduction proceeds in a conserved manner. Reducing equivalents for nucleotide reduction are ultimately provided by external sources (redoxins or formate). In most RNRs, nucleotide reduction is coupled to the oxidation of a pair of active-site cysteines, which are subsequently reduced by thioredoxin, thioredoxin reductase, and

NADPH. Some class III RNRs do not have this conserved cysteine pair, and they use formate as the external reductant (Wei et al., 2014b).

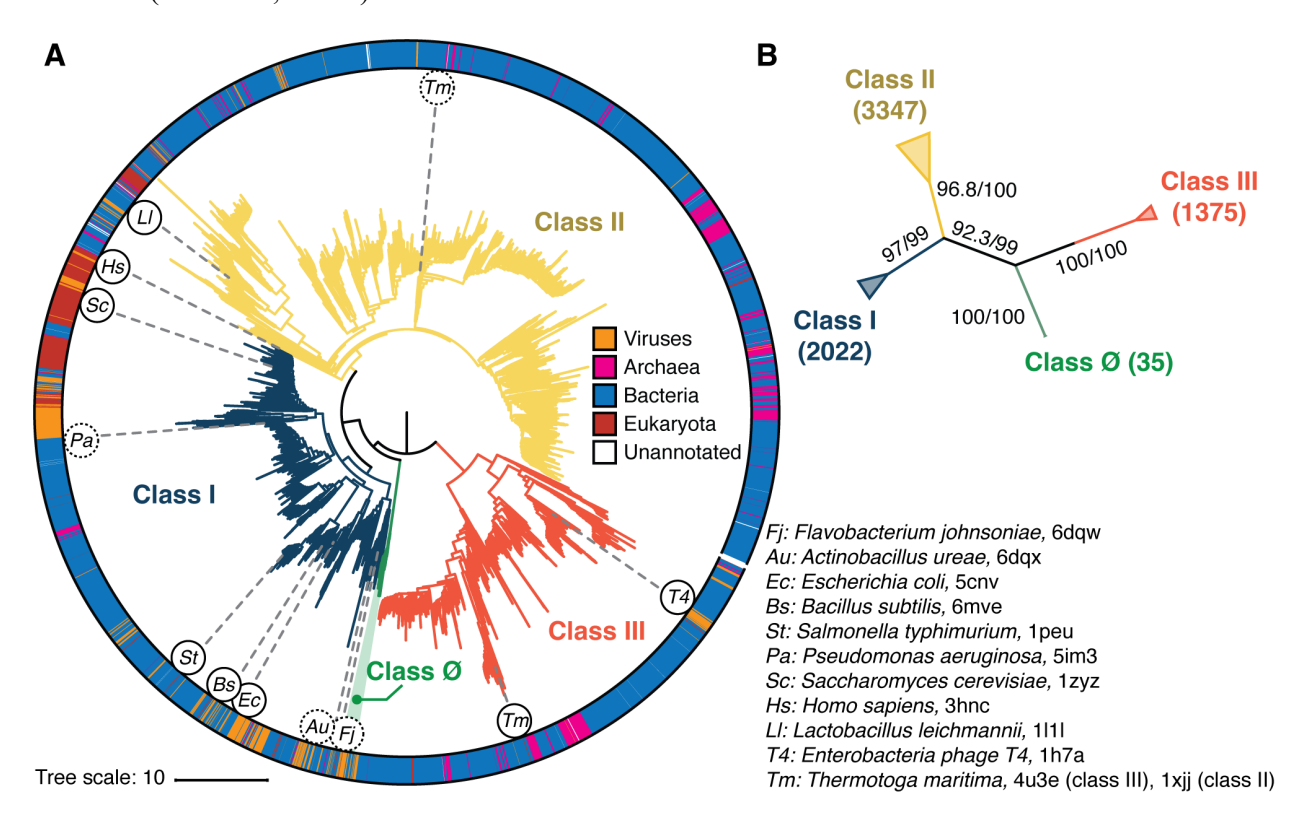
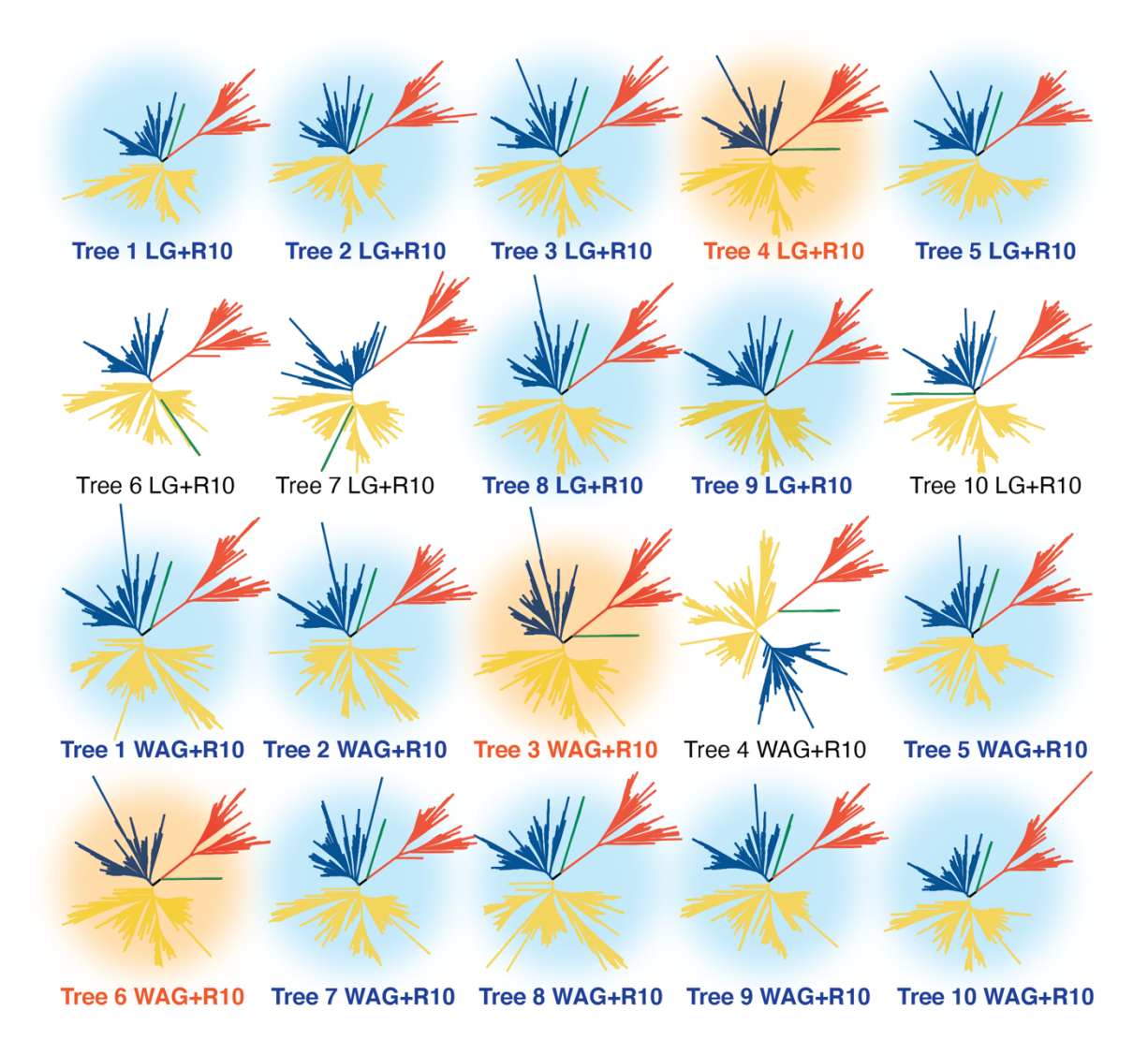
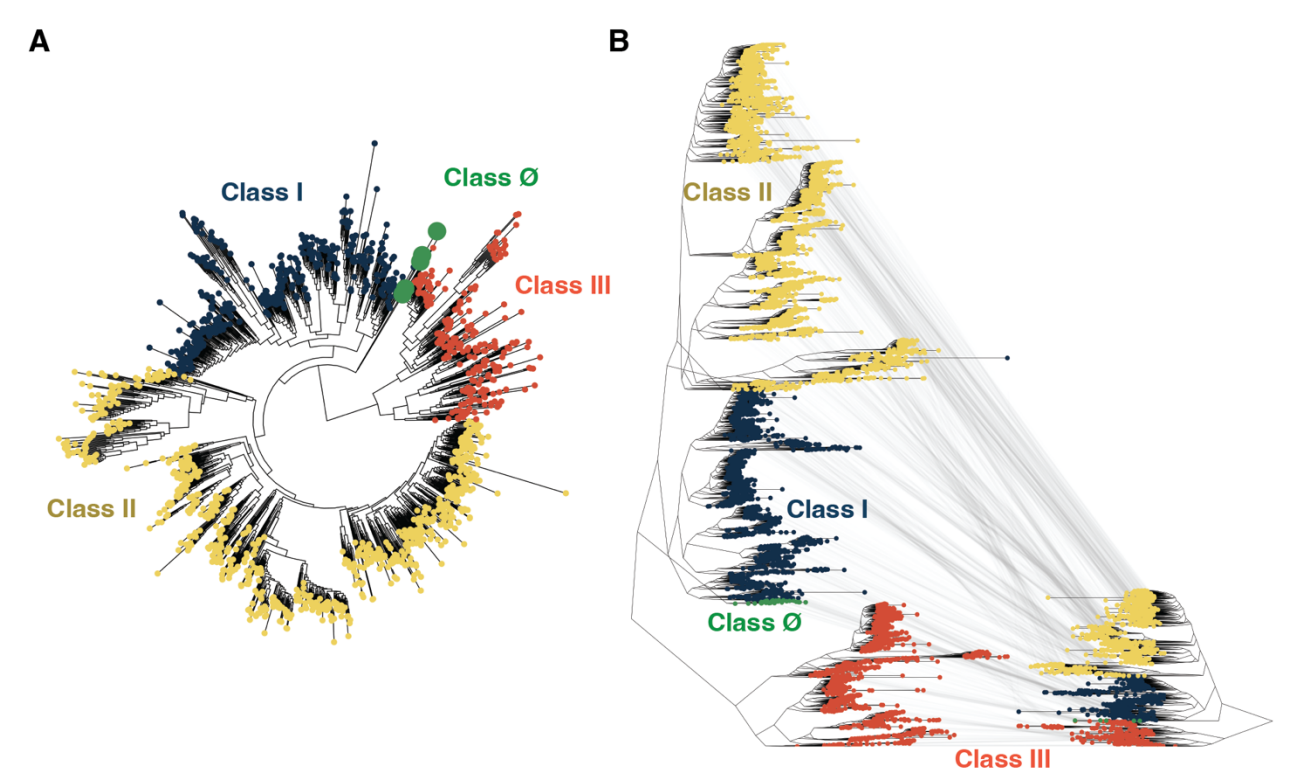


Figure 2. Phylogenetic reconstruction of the RNR superfamily. (A) A representative phylogeny of 6779 extant RNR  $\alpha$  sequences rooted at the midpoint. The superfamily forms four distinct lineages, with the three major clades (blue, yellow, red) corresponding to the three biochemically known classes I-III. Class III is the most distantly related clade (red). A small ancestral clade (green) forms an outgroup to the clades corresponding to classes I and II (blue and yellow, respectively). The scale bar represents the expected number of amino acid substitutions per site in the alignment. The taxonomic group each sequence belongs to is labelled by a color strip at the circumference. Sequences used for the structural alignment are mapped onto the tree by organism ID in circles. Organism IDs in dashed circles are  $\alpha$  sequences that were utilized in the structural alignment but were filtered in favor of more representative sequences for the tree inference and thus are not on the tree (see Methods). These structures are represented by closely related sequences with  $\geq$  80% sequence identity. (B) An unrooted representation of the RNR phylogeny with branch supports (UFboot/SH-ALRT statistics) for the placements of major lineages. Deep nodes in the RNR phylogeny are resolved with high confidence.



**Figure 2** – **figure supplement 1.** All 20 inferred phylogenies of the ribonucleotide reductase family shown in the unrooted representation. Green, red, yellow, and blue branches are clade Ø and classes III, II, and I, respectively. Trees are labeled with the respective matrices of evolution used for the phylogenetic inference. The tree shown in Figure 2 and referenced throughout this work is tree 1. Trees with the light blue background support the overall topology shown in Figure 2 of the major classes. Trees with orange background show the second most frequently observed topology, where the midpoint places the class Ø clade ancestral to the class III clade. The four trees without a colored background cannot be categorized into either of the previously described topologies.



**Figure 2 – figure supplement 2.** Tree inference is robust to sequence identity threshold. (**A**) Tree inference on an RNR sequence dataset with redundancy removed to 55% identity reconstructs class  $\emptyset$  sequences as ancestral to the last common ancestor of classes I and II, congruent with analyses performed at a higher redundancy threshold (see Methods). (**B**) The tree shown in Figure 2A (reproduced here on the left) is of identical topology to the tree inferred at a lower redundancy threshold (shown on the right). Identical sequences between the trees are mapped by grey lines. In both panels A and B, class I, II, III, and  $\emptyset$  are colored as in Figure 2.

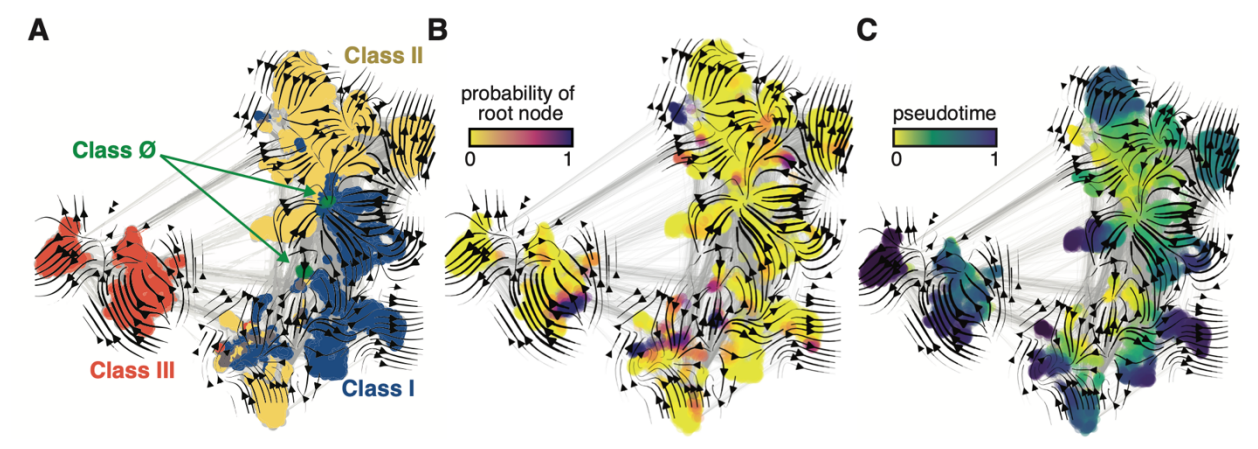


**Figure 3.** Evo-velocity analysis of the RNR superfamily. ESM-1b embedded RNR sequences were projected onto a two-dimensional vector plot, where the horizontal and vertical axes are UMAP 1 and 2, respectively. Each colored point in the plot corresponds to one of the 6779  $\alpha$  sequences from the full RNR phylogeny. (**A**) Vector field plot colored by RNR classification: clade  $\emptyset$  (green), class I (blue), class II (yellow), class III (red). (**B**) Vector field plot colored by the probability of a sequence being a root of the sequence space, where purple sequences are the most likely to represent probable roots. (**C**) Vector field plot colored by pseudotime, a proxy for phylogenetic depth. Yellow (pseudotime = 0) represents ancestral sequences and indigo (pseudotime = 1) represents sequences that have diverged the most from ancestral sequences.

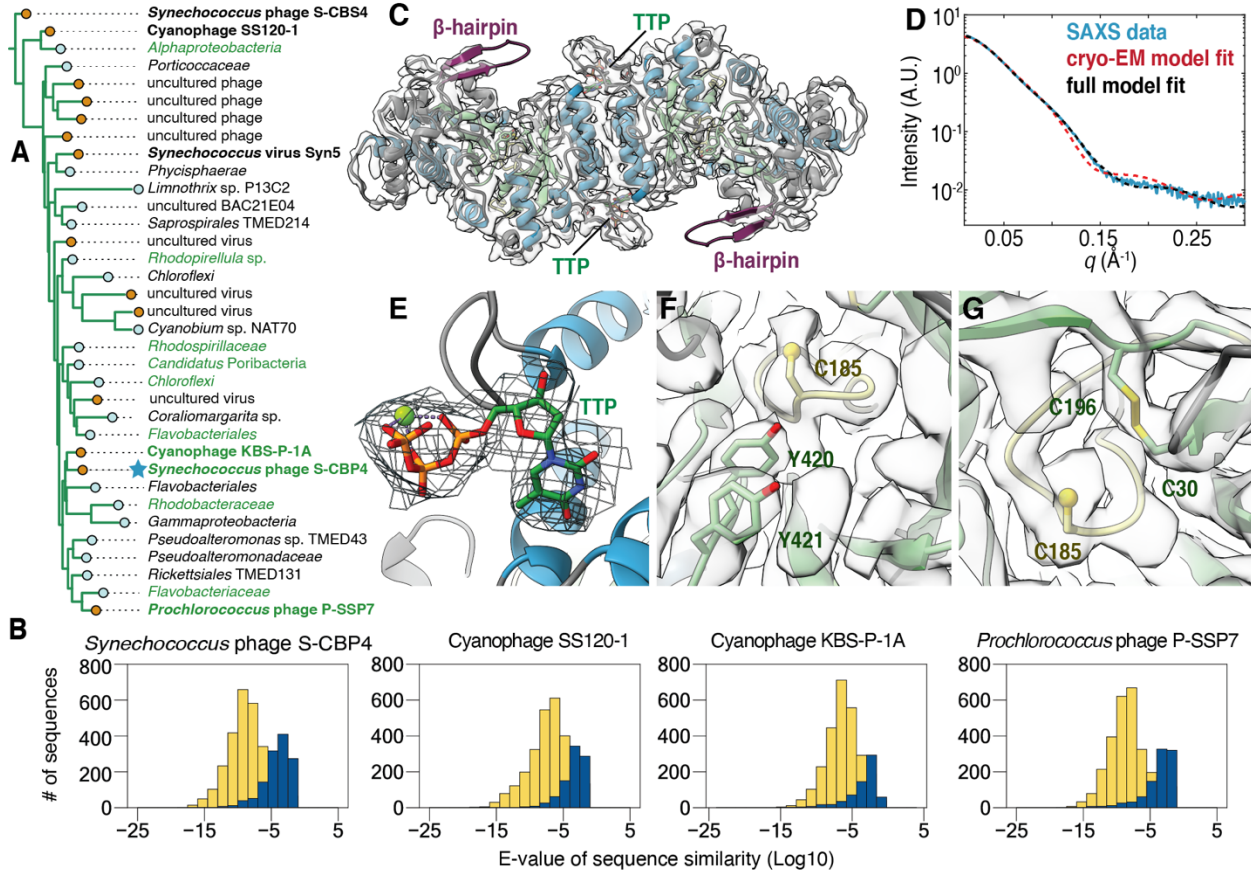


**Figure 4.** The class Ø α subunit shares similarities with both class I and II α subunits. (**A**) An expansion of the class Ø clade from the full tree in Figure 2. Cyanophage sequences in this clade are bolded. Genomes with identified photosynthetic genes, psbA and psbD, are colored in green. (**B**) Representative results from an all-vs-all pBLAST search of every class Ø sequence against all RNR α sequences from other clades. Blue bars represent number of significant hits (E-values <  $10^{-3}$ ) of the title sequence to sequences in the class I clade. Yellow bars represent number of sequences from the class II clade. Overall, the class Ø clade shares greater homology with the class II RNRs. (**C**) A 3.46-Å cryo-EM map of the *Synechococcus* phage S-CBP4 α subunit (shown at a threshold of 2.17) depicts a dimer with TTP bound at the allosteric specificity sites. The β-hairpin (violet) is a shared trait of class I and II RNRs. (**D**) Experimental SAXS profile (blue solid) of the *Synechococcus* phage S-CBP4 α subunit in the presence of 200 μM TTP, 200 mM GDP is explained well by the theoretical scattering of our cryo-EM model (red dashed). Model-data agreement is further improved by modeling the disordered N- and C-termini in AllosModFoXS (black dashed, see Methods) (Schneidman-Duhovny et al., 2010). Cryo-EM density for (**E**) TTP at the specificity site, (**F**) a stacked tyrosine dyad adjacent to the catalytic cysteine, and (**G**) the oxidized cysteine pair in the active site is shown at a threshold of 2.77.

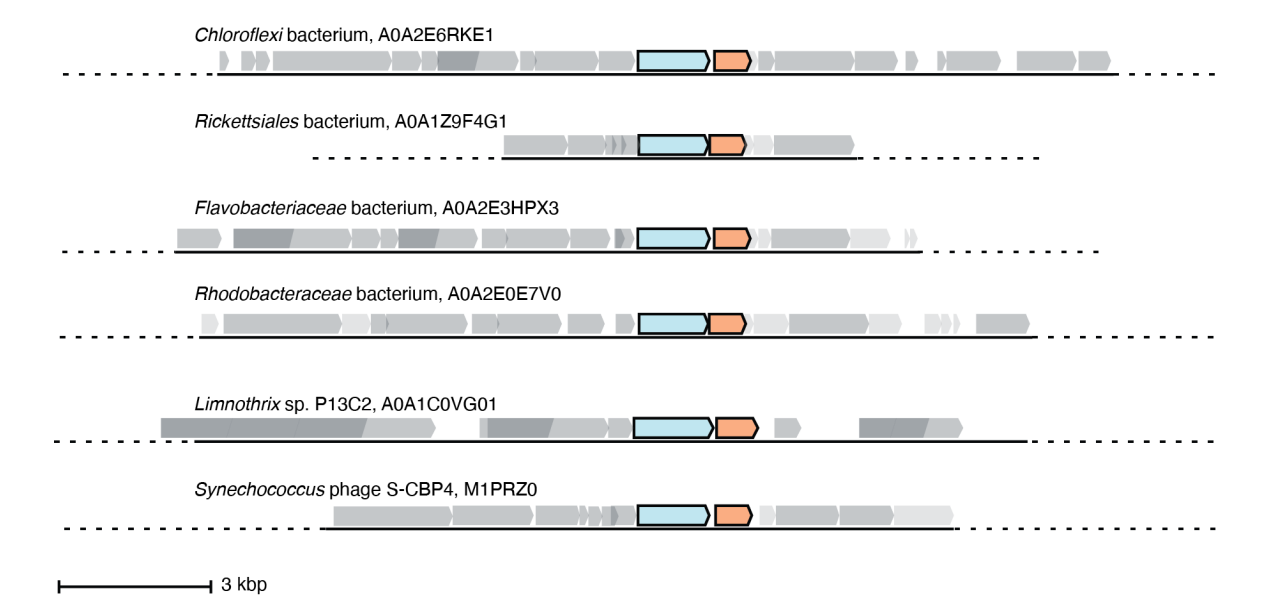


Figure 4 – figure supplement 1. Six representative operons of class Ø sequences. In sequenced organisms with high genome coverage, the  $\alpha$  gene (cyan) is followed by a gene for a small ferritin-like protein (orange). Of the 35 sequences in the class Ø clade, 24 are from sequenced genomes with greater coverage than a contig. 18 of these have annotated ferritin-like sequences (IPR009078) directly downstream of the  $\alpha$  gene in the operon, and 6 have unannotated genes that share homology with the class Ø ferritin-like gene directly downstream of the  $\alpha$  gene.

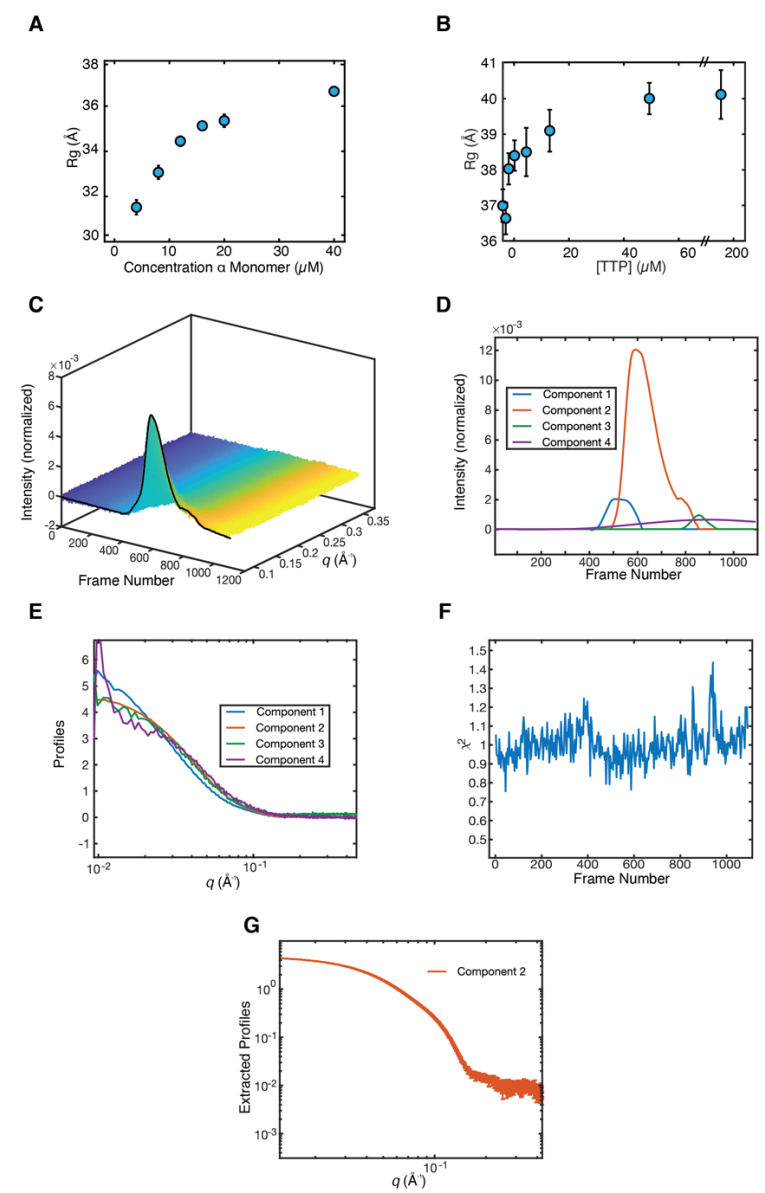
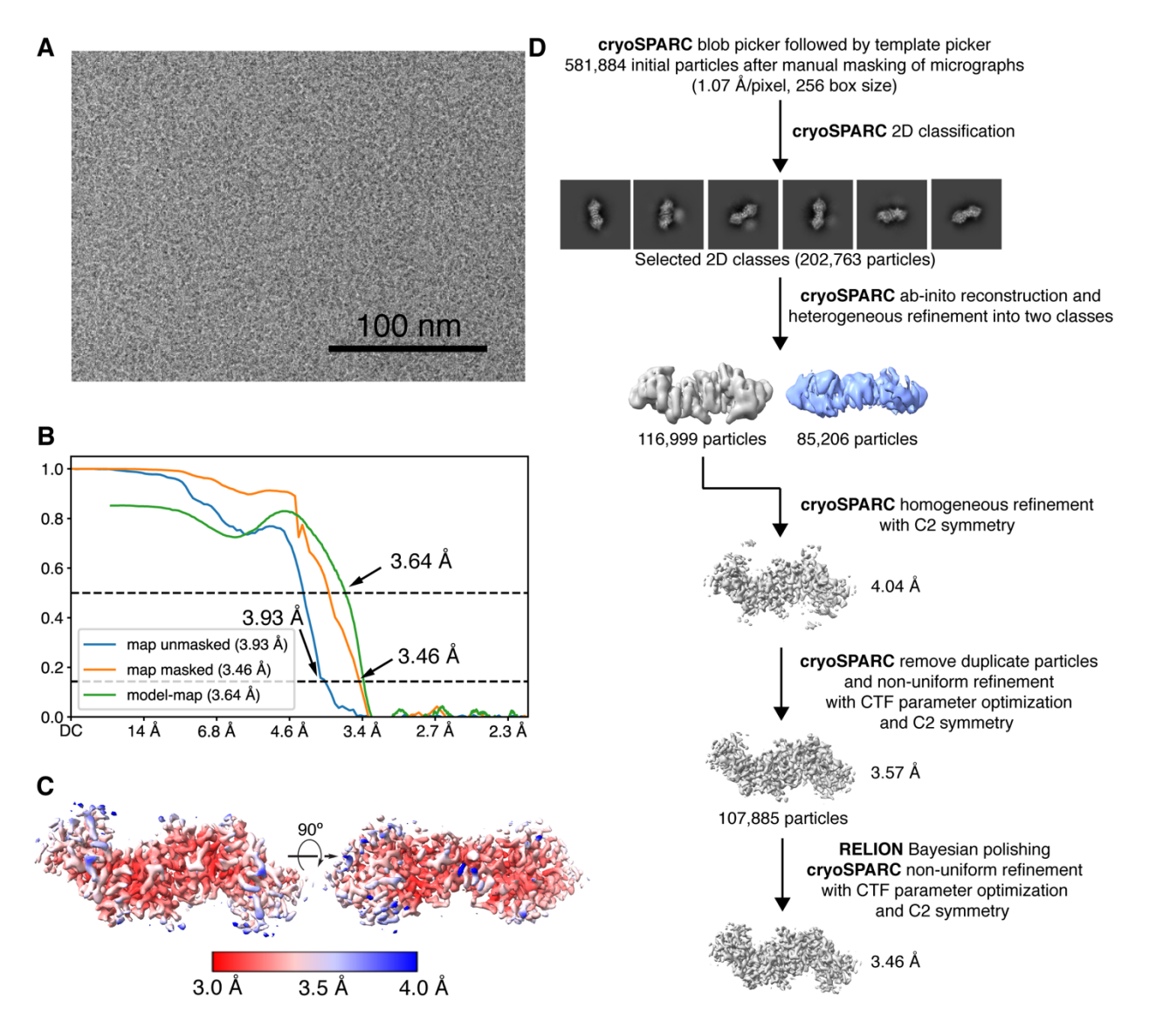
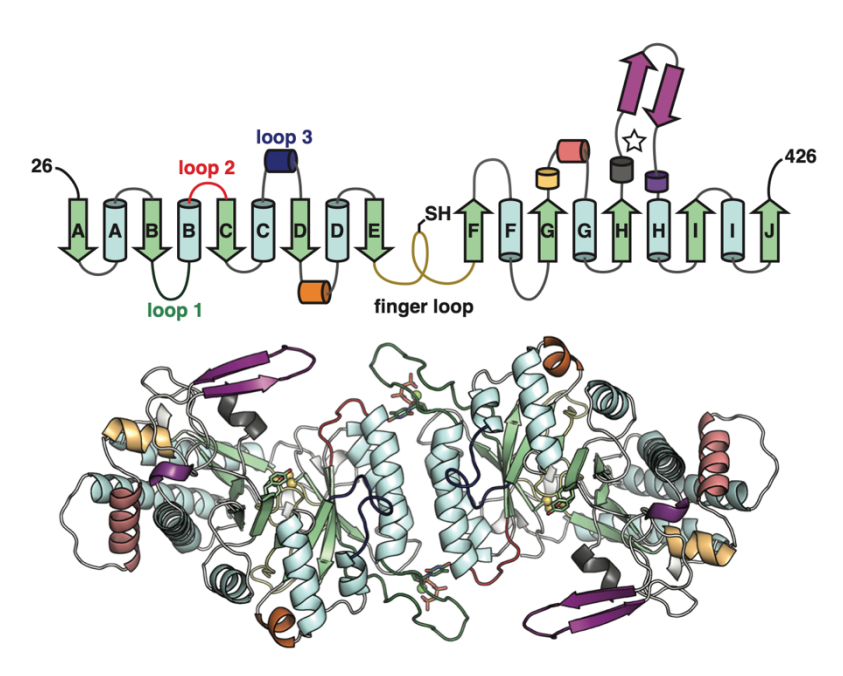


Figure 4 – figure supplement 2. Synechococcus phage S-CBP4  $\alpha$  is a stable dimer in the presence of nucleotides. (A) The radius of gyration  $(R_g)$  of Synechococcus phage S-CBP4  $\alpha$  in the absence of nucleotides as a function of protein concentration in solution shows a monomer-dimer equilibrium. (B) The  $R_g$  of 8 μM Synechococcus phage S-CBP4 α in the presence of 200 μM GDP as a function of TTP concentration in solution is consistent with the stabilization of a dimer. Error bars in panels A and B represent fitting uncertainties from Guinier analysis, and where not visible are smaller than the data marker. The theoretical  $R_g$  values of Synechococcus phage S-CBP4  $\alpha$  (based on the cryo-EM model with N- and C-termini added) are 26 Å and 37 Å, respectively, for monomer and dimer. (C) Size exclusion chromatography-coupled SAXS (SEC-SAXS) data collected on the Synechococcus phage S-CBP4 a subunit in the presence of 200 μM TTP and 200 μM GDP. Singular value decomposition (SVD) of the background-subtracted SEC-SAXS data contained 4 significant singular values. REGALS (Meisburger et al., 2021) was used to decompose the dataset into (D) elution profiles and (E) SAXS profiles for a sloping background component (purple), a minor aggregate component (blue), a protein component (red), and one trailing component (green) representing buffer mismatch and radiation damage. The presence of a minor aggregate species explains the slightly elevated  $R_g$  values observed in panel B. (F) Residuals of REGALS decomposition from SEC-SAXS dataset (G) Extracted SAXS profile for the Synechococcus phage S-CBP4 α dimer shown in Figure 4D.



**Figure 4 – figure supplement 3.** Cryo-EM image processing workflow for reconstructing the 102 kDa *Synechococcus* phage S-CBP4  $\alpha_2$  dimer. (**A**) Representative micrograph used in processing. (**B**) Fourier shell correlation (FSC) curves for the final map with and without mask reported by cryoSPARC shown as blue and orange curves. The model-map FSC curve (green) was calculated for the deposited model (PDB: 7urg) and the sharpened map using PHENIX. (**C**) Local resolution estimation computed in cryoSPARC for the final map. (**D**) Data processing scheme used to obtain the final map.



**Figure 4** – **figure supplement 4.** The class  $\emptyset$   $\alpha$  subunit features the most minimal RNR architecture discovered to-date. Top: Topology of the *Synechococcus* phage S-CBP4  $\alpha$  subunit monomer based on the cryo-EM model the minimal components of the RNR catalytic barrel colored as in Figure 1A. Only a few insertions are observed in the class  $\emptyset$   $\alpha$  subunit (yellow orange, orange, and violet secondary structures). Bottom: The cryo-EM model of the *Synechococcus* phage S-CBP4  $\alpha$  dimer with the same coloring as above.

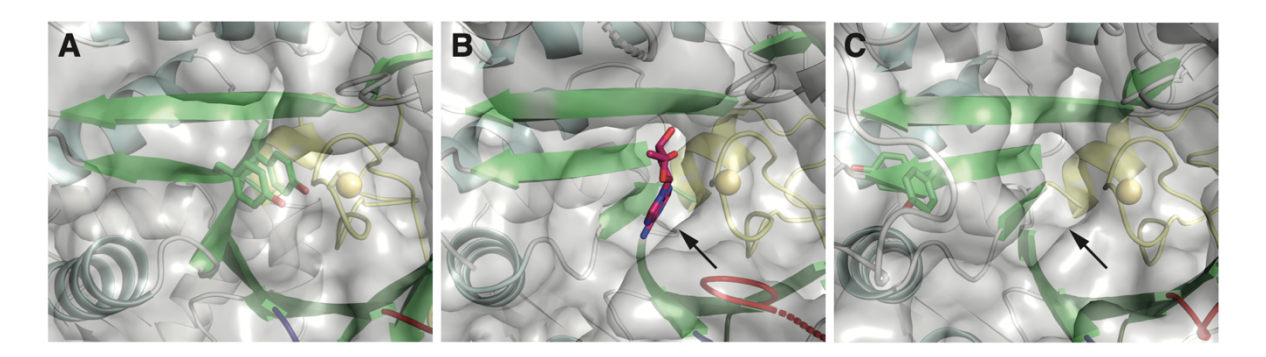


**Figure 4** – **figure supplement 5.** One structural difference between class I and II α subunits is the packing of  $\beta J$  residues next to the catalytic cysteine on the finger loop (yellow). (**A**) Class I RNRs contain a double tyrosine motif (green sticks) on the  $\beta J$  strand of the barrel. When stacked, the YY dyad packs against the finger loop, such that it is poised for PCET with the catalytic cysteine (yellow sphere). Shown here is the crystal structure of the *Escherichia coli* class Ia RNR (PDB: 5cns) (Zimanyi et al., 2016). (**B**) In structures of class II RNRs (Larsson et al., 2010; Sintchak et al., 2002), there is a binding pocket (indicated by the arrow) for the adenosyl group (magenta sticks) of the AdoCbl cofactor in the space adjacent to the finger loop (yellow). Shown here is the crystal structure of *Thermotoga maritima* class II RNR (ODB: 3000). This binding pocket is also found in apo structures that lack the cofactor. (**C**) The double tyrosine motif is also found in the  $\beta J$  strand of some class II sequences. However, AlphaFold2 prediction of these sequences suggests that the tyrosines are unstacked and placed outside of the binding pocket for the adenosyl group (indicated by the arrow). Shown here is the predicted model for the class II RNR from *Thermaerobacter marianensis* (Uniprot: E6SMJ2).

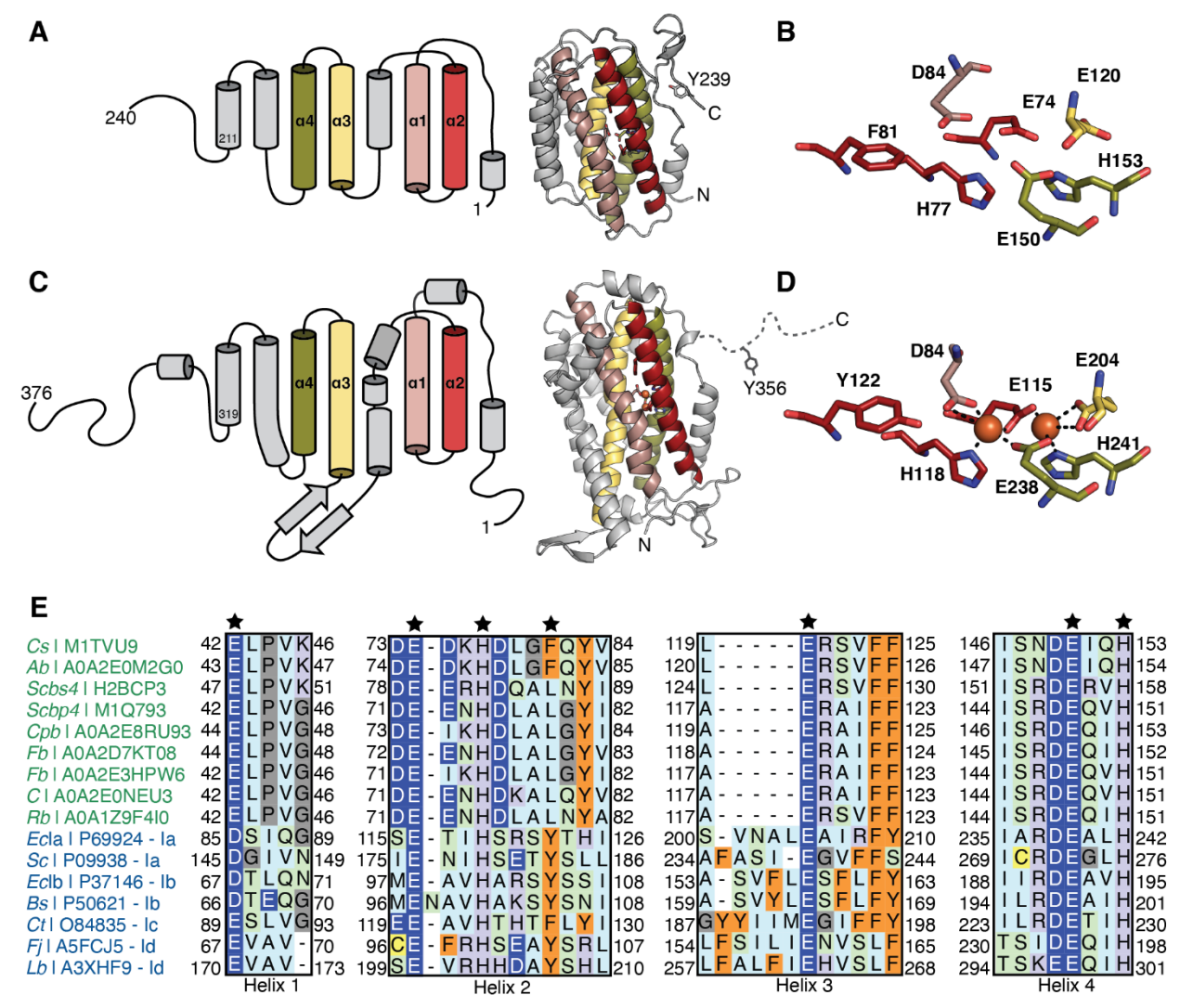


Figure 4 – figure supplement 6. Comparison of class  $\emptyset$  ferritin-like proteins with class I RNR  $\beta$  subunits. The four-helical bundle of the ferritin fold is colored in red, pink, yellow, and olive. (A) Topology (left) of an AlphaFold2 model (right) of a representative class Ø ferritin-like protein (Unitprot: M1TVU9) and (B) a close-up of the residues that would putatively form the metal-binding motif. In this sequence, a redoxinert phenylalanine (F81) is found in the i+4 position from first histidine in the motif (H77). (C) Topology (left) of the crystal structure (right) of the E. coli class Ia RNR β subunit (PDB: 1piy) and (**D**) a close-up of the residues that form the diiron center. The site of the radical is a tyrosine (Y122) in the i+4 position from the first histidine in the motif (H118). (E) Sequence alignment of representative class Ø ferritin-like protein and class I RNR β subunits. Class Ø colored in green: Cs. Cyanophage SS120-1; Ab, Alphaproteobacteria bacterium; Scbs4, Synechococcus phage S-CBS4; Scbp4, Synechococcus phage S-CBP4; Cpb, Candidatus Poribacteria bacterium; Fb, Flavobacteriales bacterium; Fb, Flavobacteriaceae bacterium; C, Coraliomargarita sp.: Rb. Rickettsiales bacterium TMED131. Class I colored in blue: Class Ia: Ecla. Escherichia coli (strain K12); Sc. Saccharomyces cerevisiae (strain ATCC 204508 / S288c). Class Ib: EcIb, Escherichia coli (strain K12); Bs, Bacillus subtilis (strain 168). Class Ic Ct Chlamydia trachomatis (strain D/UW-3/Cx). Class Id: Fj Flavobacterium johnsoniae (strain ATCC 17061); Lb, Leeuwenhoekiella blandensis (strain CECT 7118). A conserved E/D and EXXH metal-binding motif is observed in each helical pair (1 + 2; 3 + 4). The i+4 position from the histidine in helix 2 is Phe or Leu in class  $\emptyset$  ferritin-like proteins, much like in class Ic β subunits.